iScience

CellPress
OPEN ACCESS

Article

Single-Chain Lanthanide Luminescence Biosensors for Cell-Based Imaging and Screening of Protein-Protein Interactions

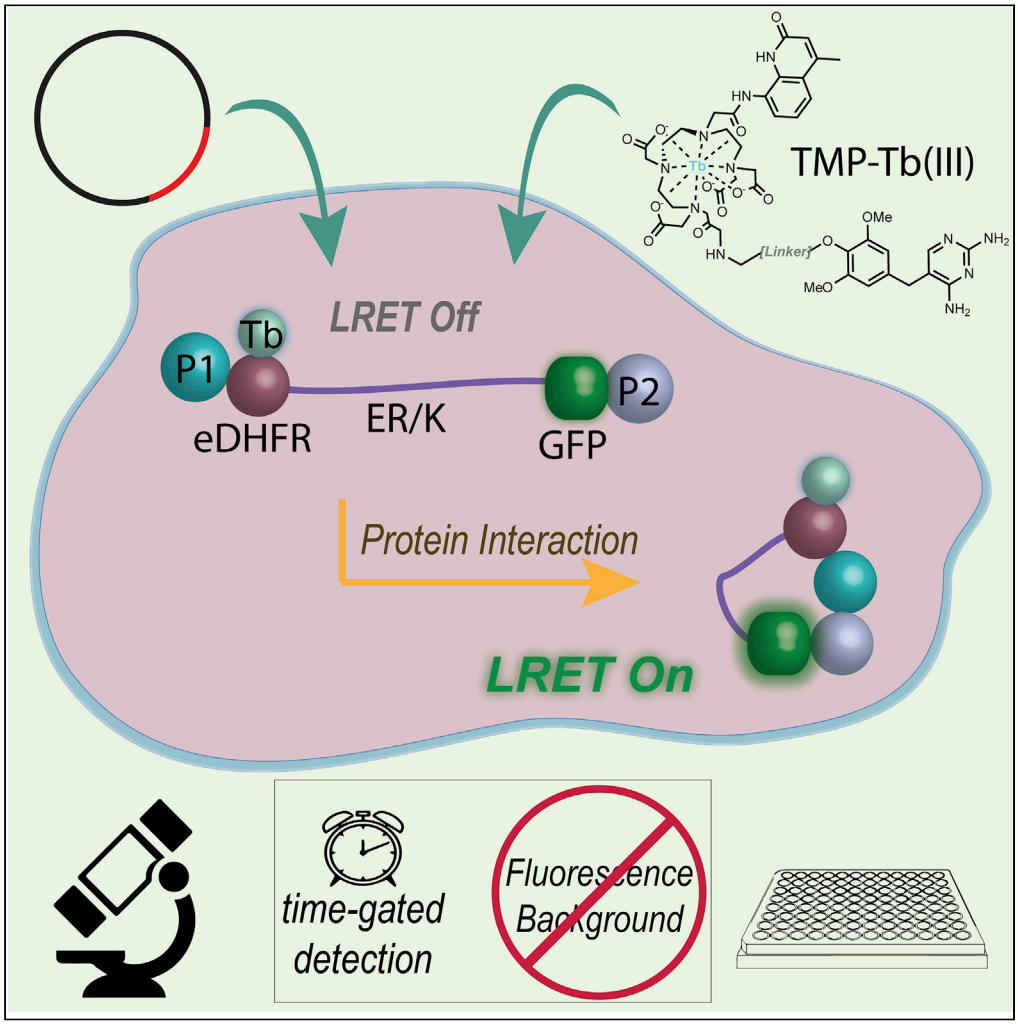

Ting Chen, Ha Pham, Ali Mohamadi, Lawrence W. Miller

lwm2006@uic.edu

HIGHLIGHTS

Non-invasive, microscopic imaging or screening of protein-protein interactions

Intracellular assembly of sensor polypeptides with luminescent Tb(III) complexes

High dynamic range with time-gated detection of Tb(III)-to-GFP sensitized emission

Chen et al., iScience *23*, 101533
September 25, 2020
https://doi.org/10.1016/j.isci.2020.101533

iScience

CellPress
OPEN ACCESS

Article

Single-Chain Lanthanide Luminescence Biosensors for Cell-Based Imaging and Screening of Protein-Protein Interactions

Ting Chen,[1] Ha Pham,[1] Ali Mohamadi,[1] and Lawrence W. Miller[1,2,*]

SUMMARY

Lanthanide-based, Förster resonance energy transfer (LRET) biosensors enabled sensitive, time-gated luminescence (TGL) imaging or multiwell plate analysis of protein-protein interactions (PPIs) in living cells. We prepared stable cell lines that expressed polypeptides composed of an alpha helical linker flanked by a Tb(III) complex-binding domain, GFP, and two interacting domains at each terminus. The PPIs examined included those between FKBP12 and the rapamycin-binding domain of m-Tor (FRB) and between p53 (1–92) and HDM2 (1–128). TGL microscopy revealed dramatic differences (>500%) in donor- or acceptor-denominated, Tb(III)-to-GFP LRET ratios between open (unbound) and closed (bound) states of the biosensors. We observed much larger signal changes (>2,500%) and Z′-factors of 0.5 or more when we grew cells in 96- or 384-well plates and analyzed PPI changes using a TGL plate reader. The modular design and exceptional dynamic range of lanthanide-based LRET biosensors will facilitate versatile imaging and cell-based screening of PPIs.

INTRODUCTION

Fluorescence-based methods that enable the imaging or analysis of protein-protein interactions (PPIs) directly in living cells are critical tools for fundamental biological research and drug discovery (Specht et al., 2017). PPIs regulate nearly all biological processes, and cell-based methods of study are required because PPIs are often weak, occur transiently in pairs or larger complexes, exist within large and overlapping biochemical networks, and often exert their function only when sequestered in distinct sub-cellular locations (Pawson and Nash, 2003). Mechanistic studies benefit from live-cell microscopy with genetically encoded fluorescent proteins (FPs) that can capture the spatial and temporal dynamics of PPIs relative to cells' response to stimuli or changes in phenotype (Piston and Kremers, 2007; Welch et al., 2011) Efforts to discover drugs that inhibit or activate PPIs are aided by cell-based screens and counter-assays that utilize multiwell plate readers and that can be used to evaluate hits or leads for cytotoxicity, membrane permeability, or off-target effects (Fletcher and Hamilton, 2007; Korn and Krausz, 2007; Scott et al., 2016).

PPIs are most commonly imaged in cells using FP-based biosensors that rely on the phenomenon of Förster resonance energy transfer (FRET) to transduce biochemical events into changes in fluorescence intensity, wavelength, or lifetime (Specht et al., 2017; Welch et al., 2011). FRET is non-radiative, dipole-dipole energy transfer from a donor fluorophore to a nearby (usually closer than 10 nm) acceptor species that has an absorption spectrum that overlaps the donor's emission spectrum (Piston and Kremers, 2007). FRET-based imaging of PPIs in live cells can be achieved with a so-called dual-chain biosensor configuration by expressing the binding partners as genetic fusions to appropriately paired FP donors and acceptors such as cyan and yellow (CFP and YFP) or green and red (GFP and RFP). Interaction of the fusion proteins results in an increase in FRET, which may be observed as a reduction in the emission intensity or lifetime of the donor and a concomitant increase in donor-sensitized, acceptor emission. Alternatively, single-chain biosensor designs are constructed such that target analyte binding or the interaction of two affinity domains induces a conformational change that modulates intramolecular FRET efficiency between donor and acceptor (Welch et al., 2011).

Although FRET can be a powerful tool for single-cell, microscopic imaging, FRET biosensor signal changes are often subtle. Consequently, FRET-based cellular assays are not commonly used for medium-throughput

[1]Department of Chemistry, University of Illinois at Chicago, Chicago, IL, USA

[2]Lead Contact

*Correspondence: lwm2006@uic.edu

https://doi.org/10.1016/j.isci.2020.101533

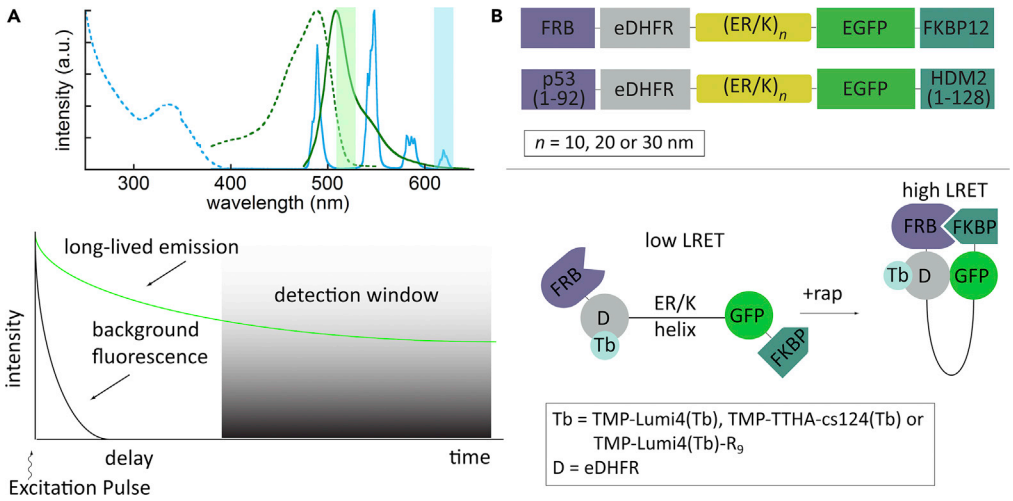

Figure 1. Single-Chain, Tb(III)-Based LRET Biosensor Design Leverages the Narrow, Multi-line Emission Spectrum and ms-Scale Excited State Lifetime of Tb(III) Complexes to Facilitate High Signal-to-Background, Time-Gated Luminescence (TGL) Detection

(A) (Top) Excitation (dotted) and emission (solid) spectra of Tb(III) (cyan) and GFP (green). Colored bars show emission band pass for detecting Tb(III) and Tb(III)-to-GFP LRET signals. (Bottom) Insertion of a microsecond-scale delay between pulsed excitation and detection enables background-free detection of Tb(III) luminescence and Tb(III)-to-GFP LRET-sensitized emission.

(B) (Top) Biosensor design. An ER/K helix motif (length 10, 20, or 30 nm) separates LRET partners and affinity pairs. (Bottom) In the absence of interaction, the ER/K helix maintains affinity and detection elements far apart, ensuring low baseline LRET signal. Stochastic breaking of helix linker permits close approach and binding of affinity domains.

or high-throughput screening (HTS) applications where large signal changes and low variability are desirable. Nevertheless, some FRET-based screening methods as well as those based on bioluminescence resonance energy transfer have been reported (Pfleger and Eidne, 2006; Song et al., 2011; Stroik et al., 2018; You et al., 2006). Non-FRET, cell-based assays for PPI discovery that have been adapted to a high-throughput rate of analysis include methods based on sub-cellular redistribution of fluorescently labeled proteins (suitable for high-content imagers) (Herce et al., 2013; Lundholt et al., 2006), reporter fragment complementation assays (e.g., split GFP, split luciferase) (Michnick et al., 2007), and reporter gene hybrid-like systems (Eyckerman et al., 2005; Petschnigg et al., 2014). However, nearly all of these available cell-based PPI assays suffer from one or more limitations, including low signal-to-background ratio (S/B) or dynamic range, high rates of false-positives/false-negatives, or protein sequestration at non-physiologic sites.

Here, we present lanthanide-based FRET (LRET) biosensors for live-cell imaging and multiwell plate analysis of PPIs. These sensors incorporate luminescent Tb(III) complexes with ms-scale excited state lifetimes as LRET donors and GFP as acceptors and are amenable to time-gated luminescence (TGL) detection. With TGL, pulsed, near-UV light is used to excite the specimen, and long-lived Tb(III) or Tb(III)-to-GFP LRET signals are captured after a brief delay (~μs) occurs, during which ns-scale sample autofluorescence and directly excited acceptor fluorescence decays (Figure 1A). We characterized sensor performance using two model systems: (1) the rapamycin-induced interaction between FK-binding protein 12 (FKBP12) and the rapamycin-binding domain of m-Tor (FRB) (Banaszynski et al., 2005) and (2) the therapeutically relevant interaction between p53 and HDM2 (Vassilev et al., 2004). Our single-chain biosensor design incorporated a rigid alpha-helical linker sequence composed of multiple repeats of approximately four glutamic acid residues alternated with approximately four arginine or lysine residues (ER/K) flanked by EGFP and *Escherichia coli* dihydrofolate reductase (eDHFR). The affinity binding elements were positioned at the N and C termini of the sensors (Figure 1B). The eDHFR domain binds with high specificity and affinity (K_D, ~1 nM) to heterodimers of trimethoprim linked to a luminescent Tb(III) complex (Rajapakse et al., 2009), permitting selective labeling of the sensor construct.

Overexpression of the biosensors in HeLa or NIH3T3 fibroblast cells followed by TGL microscopy or TGL analysis in 96- and 384-well plates enabled sensitive imaging and detection of biosensor activity.

Remarkable sensor dynamic ranges of over 500% and over 2,500% were observed for rapamycin-induced activation of FKBP12/FRB interaction in live-cell microscopic images and in 96-well plates, respectively. Statistically robust detection of FKBP12/FRB interaction and p53/HDM2 inhibition was observed in 384-well plates. The high performance seen here with model systems and a modular sensor design indicate that Tb(III)-based, single-chain FRET biosensors can be applied to analyze a wide variety of PPIs.

RESULTS AND DISCUSSION

Several noise sources reduce the dynamic range and precision of FRET imaging with FPs, hinder the ability to monitor two or more FRET pairs in a single specimen, and limit the use of FRET for cell-based HTS (Piston and Kremers, 2007; Song et al., 2011; Welch et al., 2011). Broad and overlapping excitation and emission spectra, non-specific background from sample autofluorescence, directly excited acceptor emission or library compound fluorescence (for HTS applications), and local differences in donor- and acceptor-labeled protein concentrations necessitate multi-channel image acquisition to isolate and accurately quantify biochemically relevant FRET signals. Single-chain biosensor designs maintain a 1:1 donor:acceptor ratio and allow for two-color, ratiometric measurements (FRET/donor or FRET/acceptor) to quantify FRET changes. However, single-chain sensors may fold into an Off-state conformation where the donor and acceptor labels are in close proximity or an On-state conformation where their relative dipole moments disfavor FRET, often resulting in high baseline FRET signals and dynamic ranges lower than 50% (Komatsu et al., 2011; Lam et al., 2012). Considerable efforts have been made to improve single-chain FRET biosensor dynamic range by using circularly permuted FPs to optimize fluorophore orientation (Nagai et al., 2004), mutating FPs to increase their inherent dimerization (You et al., 2006), and engineering linker sequences that better separate affinity elements and fluorophores in the low-FRET state (Allen and Zhang, 2006; Komatsu et al., 2011).

LRET (for *luminescence* or *lanthanide-based* resonance energy transfer) differs from FRET in several ways that can enhance the sensitivity and utility of PPI imaging or analysis. LRET employs luminescent complexes of lanthanide cations (Tb(III) and Eu(III), in particular) as donor chromophores in combination with FPs, organic fluorophores, or other fluorescent species as acceptors. Lanthanide excited state lifetimes are markedly longer (up to a few ms) than those of conventionally fluorescent acceptors (~ns), and these differences result in approximately equal luminescent decay times of LRET-quenched lanthanide donor emission and lanthanide-sensitized, acceptor emission (Selvin, 2002). These long decay times facilitate TGL detection, in which a brief delay (~μs) is inserted between pulsed excitation and signal acquisition that nearly eliminates ns-scale background including autofluorescence from cells or sample containers, fluorescence from library compounds, and directly excited, sensitized acceptor emission (Figure 1A). Moreover, the multiple, narrow and well-separated emission bands of Tb(III) or Eu(III) are easily separated from sensitized acceptor emission signals and can be used to excite differently colored fluorescent acceptors, permitting highly multiplexed LRET-based analyses (Hildebrandt et al., 2014). For these reasons, TGL assays using lanthanide probes and commercially available, multiwell plate readers are used extensively for drug discovery (HTS) and clinical diagnostics (Zwier et al., 2014).

Recent years have seen efforts to engineer lanthanide complexes for cell-based, TGL biosensing and imaging applications including sensing of pH, metal ions, nucleic acids, enzymatic activities, and PPIs (Aulsebrook et al., 2018; Mathieu et al., 2018; New et al., 2010; Rajendran et al., 2014; Zhang et al., 2018). A number of studies reported proof-of-concept LRET microscopic imaging of molecular interactions between Tb(III)- or Eu(III)-labeled and fluorophore-labeled species on cell surfaces including G-protein-coupled receptor (GPCR) ligand binding (Delbianco et al., 2014), GPCR oligomerization (Comps-Agrar et al., 2012; Faklaris et al., 2015), cadherin interactions (Linden et al., 2015), and interactions between complementary morpholino probes in zebrafish embryos (Cho et al., 2018). LRET between Tb(III) complexes and quantum dots on cell surfaces and in zebrafish has been shown to be an effective approach to signal amplification and multiplexing (Afsari et al., 2016; Cardoso Dos Santos et al., 2020). The Miller laboratory first demonstrated TGL imaging of intracellular PPIs. The chimeric proteins eDHFR/ZO-1 (19–113) and EGFP/claudin-1 (187–211) were expressed in MDCKII cells. The eDHFR ligand, TMP, covalently coupled to the Tb(III) complex, Lumi4 (TMP-Lumi4) was introduced into the cytoplasm, and interactions between TMP-Lumi4-labeled ZO1-eDHFR and EGFP-claudin were imaged with a bespoke TGL microscope (Rajapakse et al., 2010).

LRET Biosensor Design

In this study, we aimed to develop single-chain, Tb(III)-based biosensors for both imaging and cell-based screening of PPIs, but we were concerned about high baseline signals. During the ms-scale, excited state

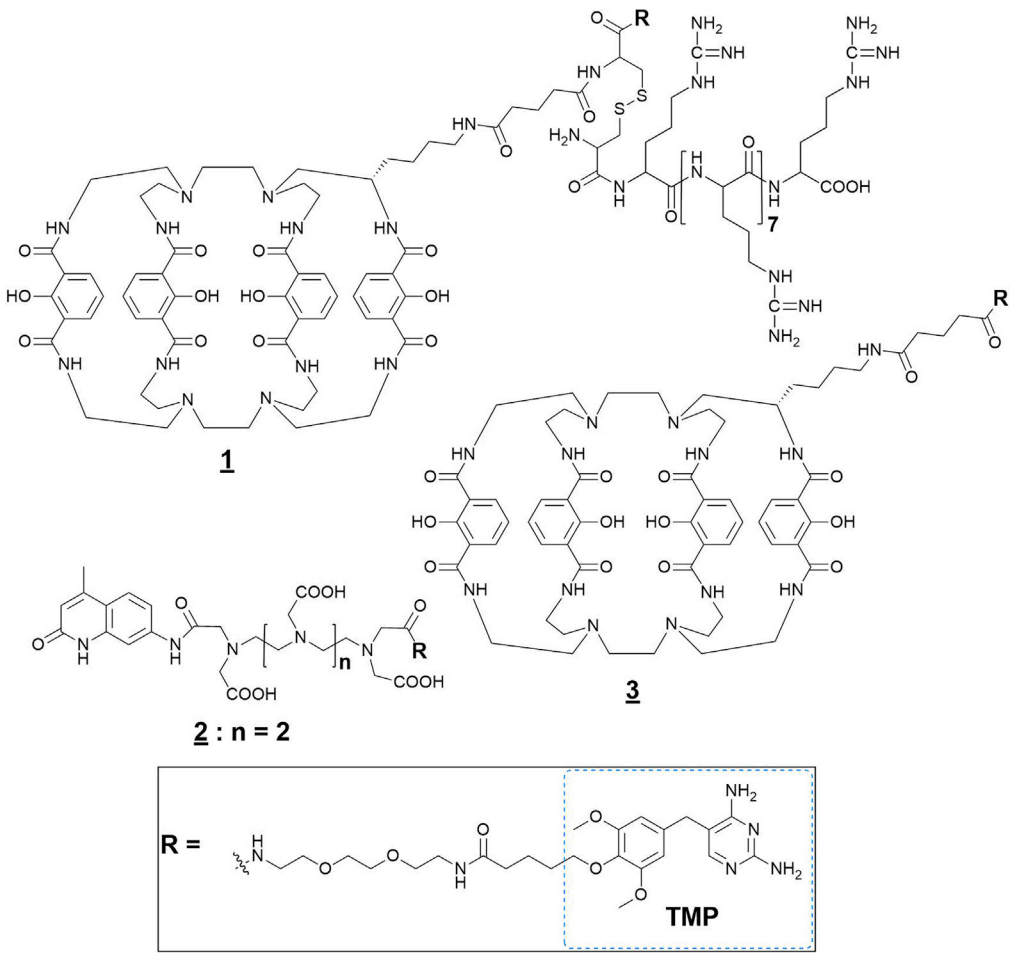

Figure 2. Heterodimers of Trimethoprim (TMP) and Luminescent Tb(III) Complexes Label Sensors Via Stable Binding to *Escherichia Coli* Dihydrofolate Reductase (eDHFR) Domains and Serve as Effective LRET Donors

Compounds used in this study and the photophysical properties of their Tb(III) complexes including longest wavelength absorption maximum (λ_{max}), absorption coefficient at λ_{max} (ϵ), overall quantum yield ($\varphi_{Overall}$), metal-centered quantum yield (φ_{Tb}), lifetime (τ), and Förster distance with EGFP ($R_{0,EGFP}$) are as follows: 1. TMP-Lumi4-R_9: λ_{max}, 340 nm; ε, 21,000 $M^{-1}cm^{-1}$; $\varphi_{Overall}$, 0.6; φ_{Tb}, 0.7; τ, 2.4 ms; $R_{0,EGFP}$, 0.48 nm. 2. TMP-TTHA-cs124: λ_{max}, 341 nm; ϵ, 10,000 $M^{-1}cm^{-1}$; $\varphi_{Overall}$, 0.21; φ_{Tb}, 0.6; τ, 1.6 ms; $R_{0,EGFP}$, 0.47 nm. 3. TMP-Lumi4: photophysical properties same as for TMP-Lumi4-R_9.

lifetimes of Tb(III) or Eu(III), many sensor conformations can be sampled, some of which might bring the donor and acceptor close to one another. Owing to their highly spiked emission peaks, lanthanide LRET donors are typically characterized by large overlap integrals and consequently high R_0 values (the donor-acceptor distance at which energy transfer efficiency is 50%). Furthermore, lanthanide-sensitized acceptor emission can often be detected at distances greater than $2 \times R_0$ because of high S/B TGL detection (Hildebrandt et al., 2014; Selvin, 1996). The R_0 values of the Tb(III) complexes paired with EGFP in this study are in the 5 nm range (Figure 2, see Transparent Methods for calculations), which would provide a detectable distance of about 10 nm ($2 \times R_0$). To minimize baseline LRET signals, we incorporated a linker into our sensor design that consists of an alternating sequence of approximately four glutamic acid residues followed by approximately four arginine or lysine residues [$E_4(R/K)_4$ or ER/K linker].

As reported, the ER/K linker adopts a rigid, alpha-helical geometry in solution (Sivaramakrishnan and Spudich, 2011). However, it was speculated that the ER/K helix can break stochastically, permitting close approach of elements positioned on either end. Thus, insertion of the ER/K sequence between affinity binding elements and FRET partners can yield a biosensor with low baseline FRET because the donor and acceptor are held far apart in the Off-state, yet the ends can still bind to one another. As the affinity

elements are tethered together, their effective concentration depends only on linker length and is independent of solution concentration. The overall fraction of an ER/K biosensor in the closed or On-state depends only on the K_D of the affinity elements and linker length. Consequently, PPIs may be observed and analyzed even when the overall sensor concentration is far below the K_D (Swanson and Sivaramakrishnan, 2014),

Another important component of the sensor design is the eDHFR domain that binds to TMP-linked small molecules with high affinity (K_D, ~1 nM) and selectivity (Miller et al., 2005). In our prior work, we have shown that TMP-coupled Tb(III) complexes bind effectively to eDHFR fusion proteins *in vitro* (Rajapakse et al., 2009), in lysates (Yapici et al., 2012) and in living mammalian cells (Rajapakse et al., 2010). Given the high affinities of TMP for eDHFR and of commonly used chelators for Tb(III) ($K_A > 10^{14}\ M^{-1}$) (Selvin, 1996), assemblies of eDHFR and TMP-Tb(III) remain stable in cells or at high dilution in challenging environments. When conjugated to arginine-rich, cell-penetrating peptides such as Tat or oligoarginine, TMP-Tb(III) complex heterodimers directly enter the cytoplasm of live cells, effectively label eDHFR targets in the cytoplasm or nucleus, and remain luminescent for hours (Mohandessi et al., 2012; Zou et al., 2015). In this study we used three different TMP-Tb(III) complex heterodimers (Figure 2). For intracellular studies, we employed TMP linked to the Tb(III) complex, Lumi4, and nine arginines (TMP-Lumi4-R_9, 1) (Mohandessi et al., 2012). For plate reader studies in cell lysates, we employed two different probes including a heterodimer of TMP and the sensitized Tb(III) complex cs124-TTHA (2) and also a TMP-Lumi4 heterodimer that lacked the cell-penetrating nonaarginine peptide (3) (Rajapakse et al., 2009).

TGL Microscopy of Biosensors in Live Cells

NIH3T3 fibroblasts were stably transfected with plasmid DNA encoding a single fusion protein under control of a tet-responsive promoter that contained the following elements (from N to C terminus): FRB, eDHFR, ER/K, EGFP, and FKBP12 (Figure 1B). We chose to examine the interaction between FKBP12 and FRB because it provides a well-understood and controllable system for evaluating sensor performance (Banaszynski et al., 2005). The timing and degree of binding can be controlled by titrating the system with the desired amount of the immunophilin, rapamycin, which mediates FKBP12/FRB binding. Three stably transformed cell lines were created that expressed sensors with ER/K linker lengths of 10, 20, or 30 nm. Following overnight induction of protein expression with doxycycline, cells were incubated in culture medium containing compound 1 (12 μM, 15 min, room temperature), washed with PBS, immersed in imaging medium, and then imaged immediately (see Transparent Methods for detailed descriptions of all materials, instrumentation, experimental protocols, and data analysis).

Steady-state images of GFP fluorescence and time-gated images of Tb(III) luminescence and Tb(III)-to-GFP sensitized emission (LRET) revealed sensor distribution throughout the cytoplasm and Tb(III) probe distribution throughout the cytoplasm and nucleus (Figure 3A). We saw very little spectral bleedthrough from the Tb(III) channel into the LRET channel, and we did not observe any directly excited GFP fluorescence (because of time-gating). Consequently, we only processed the images for shade and detector offset correction and background subtraction (see Transparent Methods). We evaluated sensor response by calculating the ratios of signals observed in the time-gated LRET channel to those observed in either the time-gated Tb(III) luminescence (LRET/Tb) or steady-state GFP fluorescence (LRET/GFP) channels. It is important to note that although these calculated quantities cannot be compared with one another, they are suitable for quantifying changes in sensor conformation within the same experiment.

In a time-series image sequence of cells expressing the sensor with a 20-nm linker, the donor-denominated LRET ratio (LRET/Tb) increased to over 300% of its initial value about 15 min after rapamycin addition (Figure 3B). In the ratiometric images shown in Figure 3B, it is evident that the magnitude of the change in LRET/Tb varies from cell to cell. Likely, this occurs because sensor expression level or the amount of probe that enters a given cell can vary, and a large excess of one or the other could skew the ratio. When we averaged observations from multiple cells, we observed large increases in both LRET/Tb and the acceptor-denominated LRET ratio (LRET/GFP) in rapamycin-stimulated cells expressing biosensors bearing 10, 20, and 30 nm ER/K linkers (Figure 3C). The dynamic ranges of both LRET/Tb and LRET/GFP signals increased with linker length. In cells expressing FKBP12/FRB biosensors with 10-, 20-, and 30-nm ER/K linkers, the maximum observed changes in LRET/Tb were 90% (±7%; mean ± SEM), 290% (±8%), and 520% (±10%), respectively The maximum microscopically observed increases in mean LRET/GFP were 60% (±11%), 380% (±10), and 470% (±12%) for linker lengths 10, 20, and 30 nm, respectively. Notably, the

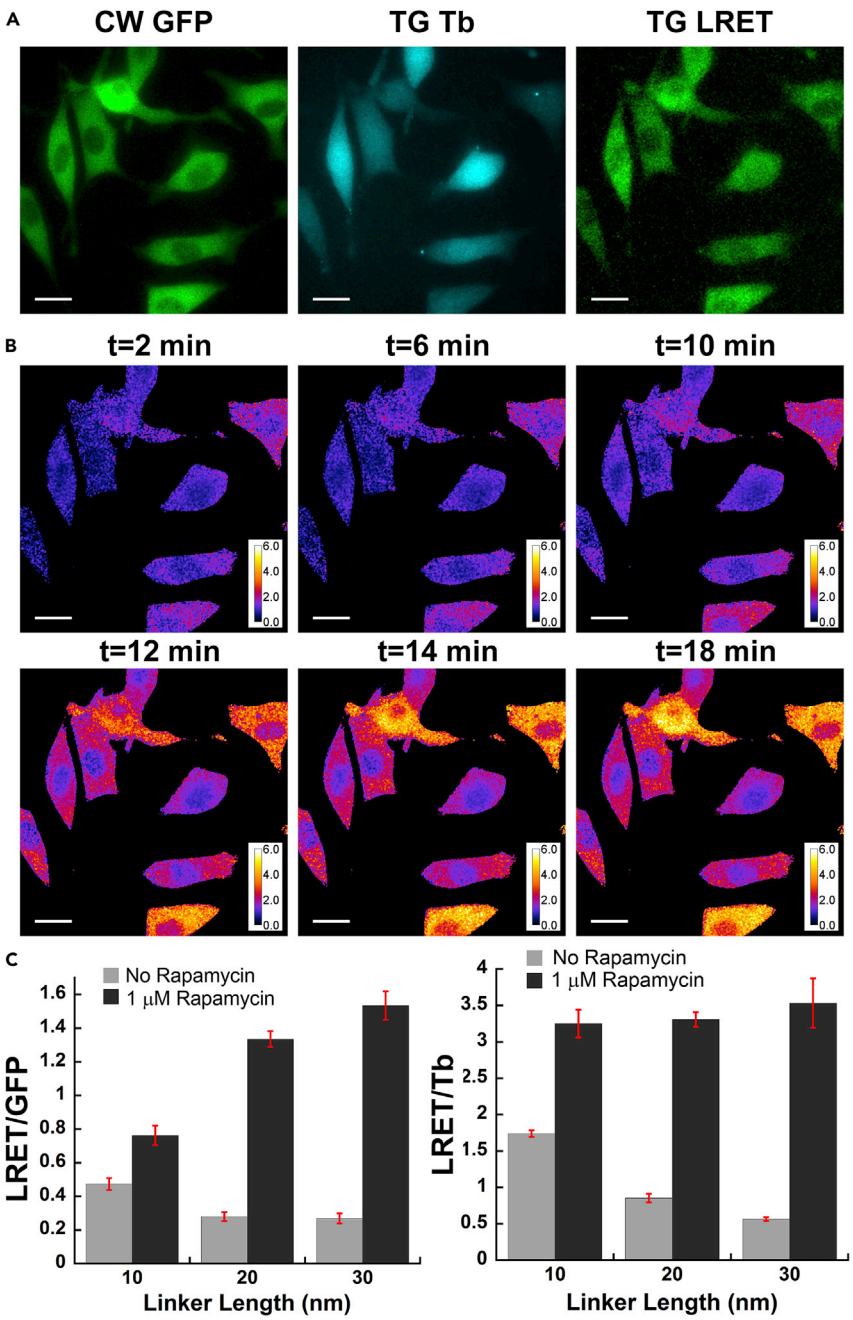

Figure 3. Time-Gated Luminescence Microscopy Enables Two-Channel, Ratiometric Imaging of LRET PPI Biosensors with High Dynamic Range

(A) Representative images of NIH3T3 fibroblasts stably expressing FRB-eDHFR-$(ER/K)_{20}$-GFP-FKBP12 approximately 20 min after stimulation with rapamycin (1 μM). Micrographs: CW GFP, steady-state GFP fluorescence (λ_{ex}, 480 ± 20 nm; λ_{em}, 535 nm ± 25 nm); TG Tb, time-gated Tb(III) luminescence (λ_{ex}, 365 nm, λ_{em}, 620 nm ± 10 nm, gate delay 10 μs); TG LRET, time-gated Tb(III)-to-GFP sensitized emission (λ_{ex}, 365 nm; λ_{em}, 520 ± 10 nm, gate delay 10 μs). Scale bars, 20 μm. TG Tb and TG LRET channel images were rendered at identical contrast.

(B) Color maps of the same cells shown in (A) depict the ratio of the TG LRET image to the TG-Tb image at various time points following rapamycin stimulation.

(C) Biosensor dynamic ranges increase with the length of ER/K linker due to reduction in baseline, or Off-State LRET signals. Bar graphs depict the mean, pixel-wise LRET/Tb or LRET/GFP ratios measured in regions of interest drawn within images of cells acquired before and 25 min after addition of rapamycin. Values given are averaged from 10 or more cells for each condition. Error bars, SEM.

LRET/GFP dynamic ranges for the single-chain FKBP12/FRB sensors with 20 and 30 nm linker lengths substantially exceeded the dynamic range of a dual-chain FKBP12/FRB sensor (LRET/GFP, 270% ± 40%; Figure S1) and were comparable to the signal enhancement previously observed with TGL LRET imaging of interactions between cytoplasmic ZO-1 and claudin-1 domains (~500%) (Rajapakse et al., 2010), GPCRs (~200%)(Comps-Agrar et al., 2012), and fluorophore-labeled morpholinos in zebrafish embryos (~1,200%) (Cho et al., 2018).

The remarkable dynamic ranges that we observed are critically dependent on the incorporation of the ER/K linker into the sensor structure. We prepared an analogous sensor that incorporated 27 repeats of the sequence EAAAK in place of the ER/K linker, FRB-eDHFR-$(EAAAK)_{20nm}$-EGFP-FKBP12. Repeats of EAAAK are known to form extended alpha helices in solution and were previously shown to enhance the functionality of independent domains when incorporated as linkers into fusion proteins (Arai et al., 2001). We observed no significant changes in LRET when rapamycin was added to NIH3T3 cells that expressed FRB-eDHFR-$(EAAAK)_{20nm}$-EGFP-FKBP12 (Figure S2). These results support the original findings of Sivaramakrishnan and Spudich (Sivaramakrishnan and Spudich, 2011) and illustrate the apparent capability of ER/K helices to reside in an extended conformation, yet permit close approach of their termini such that affinity elements at each end may bind to one another.

Detection of PPIs and Their Inhibition in Multiwell Plates

Often, conventional FRET-based detection of cellular PPIs at medium throughput (96-well plate) or high throughput (384-well plate) is impossible because of the aforementioned limitations in FRET S/N and dynamic range and the relatively small amounts of protein in each sample well (Song et al., 2011). We sought to assess the potential of our Tb(III) biosensors for detection and quantification of PPIs and their inhibition in multiwell plate format following expression in live mammalian cells. NIH3T3 cells stably expressing single-chain, FKBP/FRB biosensors (containing 20 or 30 nm ER/K linkers) were seeded into 96-well plates (40,000 cells/well) and grown overnight in medium containing doxycycline to induce protein expression. A rapamycin titration assay was first performed to obtain the optimal rapamycin concentration to induce the FRB/FKBP12 interaction. Lysis buffer containing TMP-Lumi4-Tb (Rajapakse et al., 2009) (50 nM) and serial dilutions of rapamycin (final concentration, 5 μM to 0.5 nM) was added to the wells, and the plate was incubated at room temperature for 15 min.

Following incubation, the time-gated Tb(III)-to-GFP LRET and Tb(III) emission signals were measured at 520 and 615 nm, respectively. Then, the background-subtracted, LRET/Tb ratio for each sample well was calculated according to the following:

$$\frac{S_{520} - \overline{B}_{520}}{S_{615}} \qquad \text{Equation (1)}$$

where S_{520} represents the 520 nm LRET signal from a given sample well, $\overline{B}_{520}$ represents the mean signal from blank wells (12 in this case) that contained non-expressing cells and lysis buffer solution (with 50 nM 1, no rapamycin), and S_{615} represents the 615-nm donor-only signal. A non-linear regression fit to a plot of LRET/Tb ratio versus rapamycin concentration yielded EC_{50} values of 22 ± 2 nM and 18 ± 2 nM for cells expressing biosensors with 20- or 30-nm ER/K linkers, respectively. Maximal interaction was observed at rapamycin concentrations equal to or exceeding ~100 nM (Figure S3).

To further assess the performance of our model system, we treated sensor-expressing cells grown in either 96-well or 384-well plates with lysis buffer that included 2 (final conc., 25 nM) and either rapamycin (1 μM, positive control) or vehicle (0.25% DMSO, negative control). The background-corrected LRET/Tb ratio for each sample well was obtained according to Equation 1, the mean and SD values calculated for each set of controls, and the percent increase in LRET/Tb of positive control wells relative to negative control wells (dynamic range) was calculated. An increase in dynamic range with ER/K linker length was observed in the 96-well plate data, similar to that seen in microscopy data. However, the magnitude of the measured dynamic range was substantially higher. Cells expressing FKBP12/FRB biosensors with 10-, 20-, or 30-nm ER/K linkers exhibited dynamic ranges of 160% (±7%, mean ± SD), 1,700% (±20%), and 2,500% (±20%), respectively. For all sensor constructs, the maximum observed LRET/Tb ratio was similar. However, the sensor with 10-nm ER/K linker had a higher baseline LRET signal (Figure 4A).

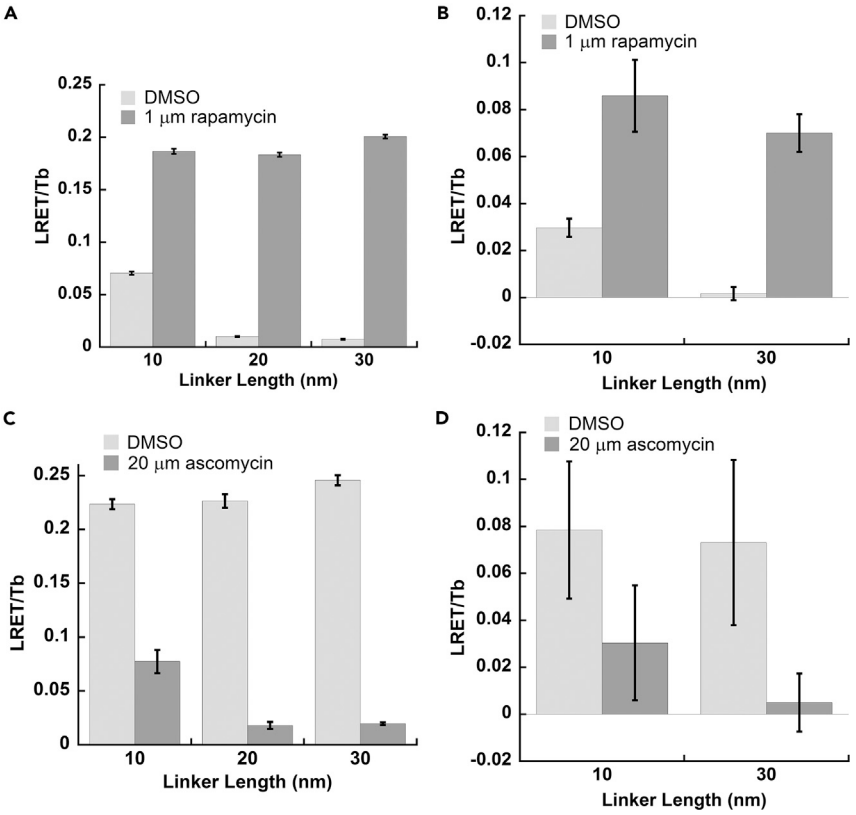

Figure 4. TGL Analysis Robustly Detects FKBP12/FRB Interaction and Its Inhibition Following Permeabilzation of Sensor-Expressing Cells Grown in Multiwell Plates

(A–D) NIH 3T3 fibroblast cells expressing FKBP/FRB sensors with varied ER/K linker lengths were seeded into 96-well (A and C) or 384-well (B and D) plates at cell densities of 40,000 or 8,000 cells/well, respectively. Following overnight incubation, cells were treated with lysis buffer containing TMP-TTHA-cs124 (25 nM). Time-gated emission signals (gate delay, 0.2 ms) at 520 nm (Tb-to-GFP LRET) and 620 nm (Tb only) were measured using a time-resolved fluorescence plate reader. (A and B) LRET/Tb ratios were substantially larger when lysis buffer contained rapamycin (1 μM). (C and D) Cells were treated with lysis buffer containing TMP-TTHA-cs124 (25 nM) and rapamycin (0.33 μM). Time-gated signals were then measured as in (A and B). Addition of ascomycin (20 μM) to lysis buffer decreased LRET/Tb emission ratios by more than 60% for all sensor linker lengths in both 96-well and 384-well plates. Bar graphs depict mean LRET/Tb ratio measured for positive controls (n = 16) and for negative controls (n = 8). Error bars, SD.

We further evaluated our system by calculating the Z′-factor, a standard quality metric for HTS assays (Iversen et al., 2006). Z′-factor is calculated from the standard deviations and means of the maximum and minimum observed signal levels obtained with positive and negative controls (i.e., without library compounds present) according to Equation 2.

$$Z' = 1 - \frac{3(\sigma_p + \sigma_n)}{\mu_p - \mu_n} \qquad \text{Equation (2)}$$

Z' can vary between -∞ and 1, with values >0.5 considered to be a very good assay, values between 0 and 0.5 considered marginal, and <0 is considered an unacceptable assay (Iversen et al., 2006). For measurement of FKBP12/FRB biosensor activation following cell permeabilization in 96-well plates, Z′ ranged from 0.7 to 0.9 for all sensors. Although these results clearly indicate a highly robust assay, high-throughput assays require the capability to measure at least 100,000 compounds per day, and this requires analysis in 384-well plates. In 384-well plates, we obtained a relatively poor Z'-factor about zero for the sensor with a 10-nm ER/K linker and a value of 0.4 for the sensor with a 30-nm ER/K linker (Figure 4B). Some variance in the data may be attributable to manual plate preparation, but a greater factor was the generally lower S/B of the raw Tb(III)-to-GFP sensitized emission signals. In 384-well plates, S/B ranged from 1–3 in positive control wells (sensor on- or closed-state), whereas the LRET S/B in positive controls of 96-well plates ranged from 5 to 7.

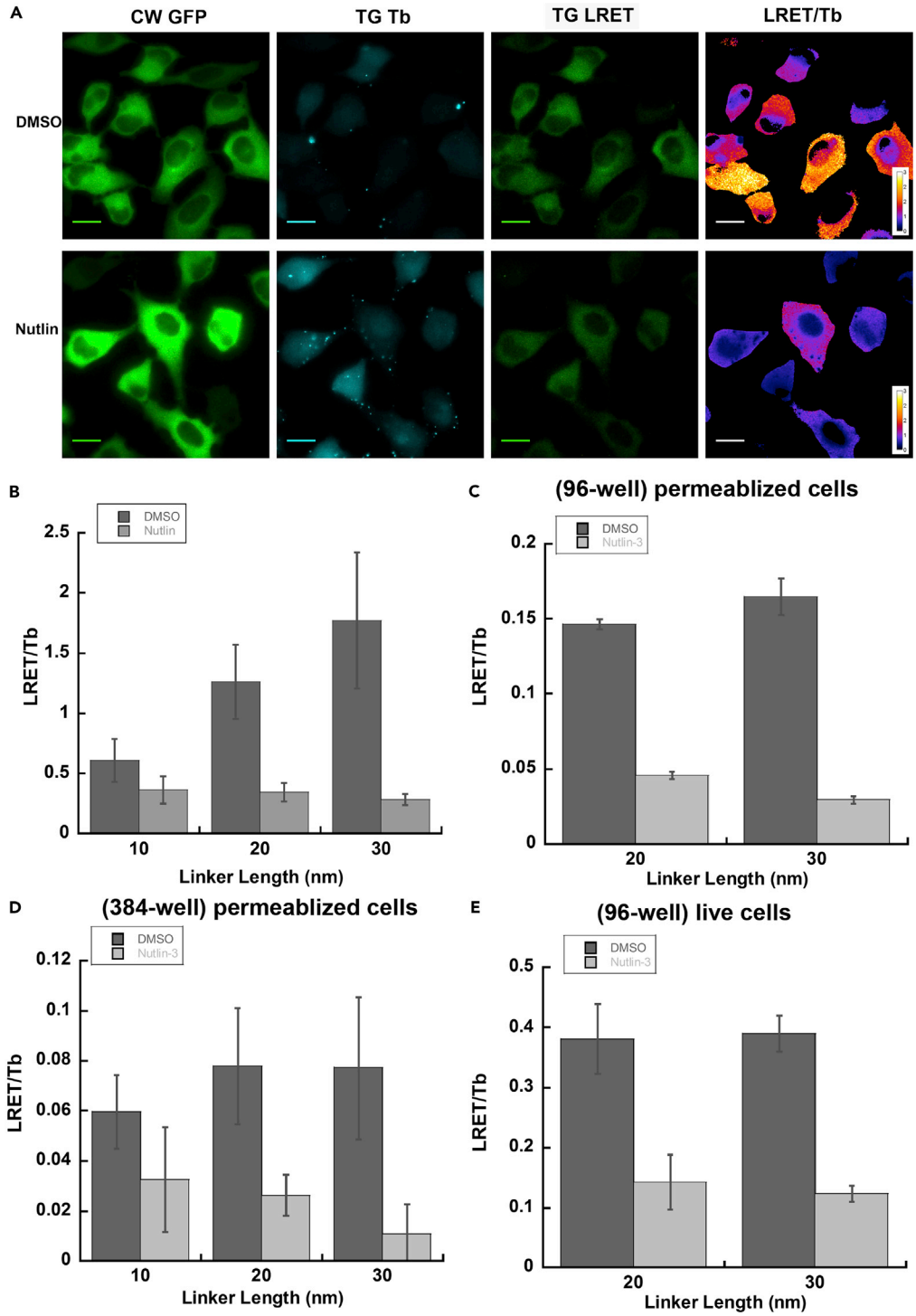

Figure 5. Large Reductions in LRET/Tb Are Observed Microscopically and in Multiwell Plates When Nutlin-3 Inhibits p53/HDM2 Interaction

(A) HeLa cells stably expressing p53(1–92)-eDHFR-$(ER/K)_{20}$-GFP-HDM2(1–128) were imaged as in Figure 3. Representative images show diminished LRET/Tb ratio in cells that were incubated with media containing Nutlin-3 (10 μM).

(B) Bar graphs depict the mean, pixel-wise LRET/Tb ratio measured in regions of interest drawn within cells. Values given are averaged from 10 or more cells for each condition. Error bars, SD.

Figure 5. *Continued*
(C–E) HeLa cells expressing p53/HDM2 sensor were grown in 96-well (C and E) or 384-well (D) plates. (C and D) Time-gated measurements were obtained following overnight induction of biosensor expression with doxycycline and addition of lysis buffer containing TMP-TTHA-cs124 (2, 50 nM) and Nutlin-3 (10 μM, positive controls) or DMSO (0.25%, negative controls). (E) Cells expressing biosensor were incubated in medium containing cell-permeable Tb complex, TMP-Lumi4-R_9 (10 μM, RT, 30 min), washed 1X PBS, and incubated in PBS containing either DMSO (negative controls) or Nutlin-3 (10 μM, positive controls). Time-gated signals were then recorded. Bar graphs depict mean LRET/Tb ratio measured for positive controls (n = 16) and negative controls (n = 16 for D and E and 8 for C). Error bars, SD.

To further evaluate the potential of Tb(III) biosensors for multiwell plate applications, we measured the effects of ascomycin as an inhibitor of the rapamycin-induced, FKBP12/FRB interaction (Banaszynski et al., 2005). Ascomycin was titrated against a constant concentration of rapamycin (0.333 μM) in permeabilized cells expressing the FKBP/FRB sensors with either 20- or 30-nm ER/K linker lengths. Non-linear fitting yielded IC_{50} values of 0.39 ± 0.05 μM for both sensors (Figure S3). Full inhibition with 20 μM ascomycin yielded LRET/Tb signal decreases of more than 60% for all ER/K linker lengths (Figures 4C and 4D). Z′ factors greater than 0.7 were obtained for all 96-well plate assay conditions, whereas large relative error yielded negative Z′ values for ascomysin inhibition in 384-well plates (Figure 4D).

Study of p53-HDM2 Interaction and Its Inhibition

The data obtained with the FKBP12/FRB model system clearly shows the strong potential of Tb(III)-based, single-chain LRET biosensors for both imaging and HTS analysis of PPIs. We further evaluated the potential of these sensors by measuring the inhibition of the interaction between p53 and HDM2. As a tumor suppressor, p53 plays a crucial role in human cancer. Its activity is controlled through a negative feedback mechanism by interaction with HDM2 (Shangary and Wang, 2009). The small molecule inhibitor of p53/HDM2 interaction, Nutlin-3, was identified in a screening campaign and represents one of the early successes of discovery efforts to find drugs that target PPIs (Shangary and Wang, 2009). We replaced the FRB domain in our original biosensors with the N-terminal 92 amino acids of p53 and replaced the FKBP12 domain with the N-terminal 128 residues of HDM2. Again, we prepared sensor constructs with 10-, 20-, and 30-nm ER/K linkers, and we stably transformed HeLa cells with the constructs for evaluation with Nutlin-3 as a positive control.

We first examined the p53/HDM2 sensor performance using microscopy. Stably transformed HeLa cells were incubated with medium containing either DMSO (0.25%, negative control) or Nutlin-3 (10 μM, positive control) at 37°C for 90 min. After incubation with cell-permeable TMP-Lumi4-R_9 (1), steady-state images of GFP fluorescence and time-gated images of Tb(III) luminescence and Tb(III)-to-GFP sensitized emission were acquired separately. A representative set of images obtained from cells expressing the p53/HDM2 sensor with a 20-nm ER/K linker clearly show a reduction in the LRET/Tb signal in cells with Nutlin-3 (Figure 5A). Quantitative image analysis once again showed that the maximum difference between On- and Off-states of the sensors increased with ER/K linker length; the mean decrease in LRET/Tb due to Nutlin-3 inhibition was measured to be 40%, 70%, and 80% (SEM, ±10%) in cells expressing sensors with 10-, 20-, and 30-nm linkers, respectively (Figure 5B).

We also performed the inhibition assays with permeabilized cells in both 96-well and 384-well plates using similar conditions to those used with the FKBP/FRB biosensors (Figures 5C and 5D). Following overnight induction of biosensor expression with doxycycline, lysis buffer containing 2 (final concentration, 50 nM) was added to wells. Nutlin-3 (final concentration, 10 μM) was also added with lysis buffer to positive control wells. Z′-factor values were calculated to determine data quality. In all assays, with cells expressing 10-nm linker biosensor, Z′-factor values were very low due to the low response from positive controls; in other words, trivial FRET changes occurred after incubation with Nutlin-3. However, Z′-factors ≥0.7 were obtained in 96-well plate assays with cells expressing 20- or 30-nm linker biosensor. In 384-well plate assays, Z′-factor values were negative in all cases.

The ability to robustly detect PPIs or their inhibition in mammalian cell culture following cell permeabilization offers distinct benefits for drug discovery and HTS. First, no protein purification is required, and it may be possible to design expression constructs where one of the affinity partners is a transmembrane protein. Second, because the sensors are expressed directly in mammalian cells, PPIs that depend on phosphorylation or other post-translational modifications may be assessed. Finally, the assay is simple, requiring only addition of lysis buffer with detection reagent and immediate readout. These capabilities critically require

TGL detection of lanthanide-based LRET as well as a single-chain biosensor design. Consider that only ~8,000 cells are present in a single well of a 384-well plate with a solution volume of 50 μL. If we assume a cell volume of 3 pL and a moderate biosensor expression level such that effective cellular concentration is 5 μM, then only sub-picomolar amounts of protein are present in a well, and the sensor concentration following cell lysis is in the low-nanomolar range. These concentrations are below the detection limits of conventional FRET and far below the K_D of most relevant PPIs. Consequently, the affinity elements must be tethered to one another and the high sensitivity of TGL detection is needed.

Plate Reader Analysis of p53-HDM2 Inhibition in Live Cells

Although PPI detection following cell permeabilization offers substantial benefits, the ability to detect PPI changes within intact, live cells could offer more biologically relevant insights as it would allow for PPI analysis in the presence of other cellular factors. Moreover, HTS assays within live cells would further assess the ability of drugs to cross the plasma membrane and their inhibition or activation characteristics within the cellular milieu. We evaluated the performance of our sensors in live cells in 96-well plates using the same, cell-permeable TMP-Lumi4-R_9 complex (3) that we used for microscopic imaging. After overnight induction in medium containing doxycycline, HeLa cells stably expressing single-chain p53/HDM2 affinity biosensors with 20- or 30-nm ER/K linker were washed and incubated in medium containing 3 (10 μM) at room temperature for 30 min. The cells were then washed one time, PBS buffer solution containing either DMSO (0.25%, negative control) or Nutlin-3 (10 μM, positive control) was added to wells, and the plate was left at room temperature for 40 min. Time-gated Tb and Tb-sensitized LRET signals were then recorded. We calculated a Z′-factor of 0.5 for cells expressing 30-nm linker biosensor (Figure 5E).

Conclusion

Single-chain LRET biosensors have a number of unique benefits for live-cell imaging and cell-based screening of PPIs. Extraordinary dynamic range stems from time-gated detection of Tb(III)-to-GFP LRET that eliminates non-specific fluorescent background and from incorporation of an alpha-helical ER/K linker that maintains Tb(III) donors and GFP acceptors far apart when the sensor is in the open configuration. These features enable dynamic visualization of PPIs in cells with TGL microscopy, robust detection of PPIs or their inhibition within intact cells grown in 96-well plates, or high-throughput detection in cell lysates in 384-well plates. In principle, it should be possible to detect interactions between a membrane protein and a cytosolic protein or between proteins that are otherwise difficult or impossible to purify. Moreover, Tb(III) can sensitize differently colored acceptors, offering the potential for multiplexed imaging or analysis. Taken together, the results presented here show that Tb(III)-based LRET biosensors offer a versatile platform technology for interrogating PPIs and their function in live cells.

Limitations of the Study

The main limitations of this study are (1) that TGL image acquisition times are substantially longer (1–2 s per channel) than those typical for wide-field fluorescence microscopy with FP biosensors (0.1–1 s per channel) and (2) the raw LRET signal observed in 384-well plates is on the borderline for acceptable HTS (S/B, ~2). Due to long excited state lifetimes, the photon output of a Tb(III) complex or Tb(III)-sensitized emission is far lower than that of conventional fluorophores. Signal levels in both imaging and HTS applications could be improved by modifying the sensors to include brighter next-generation FPs, brighter (or shorter-lifetime) lanthanide species, and/or a greater number of lanthanide donors per sensor. Continued development of the technology could also benefit from *in vitro* studies with purified sensor proteins that isolate purely biochemical and optical properties of sensor performance from those that depend on cellular factors such as expression level.

Resource Availability

Lead Contact

Further information and requests for resources and reagents should be directed to and will be fulfilled by the Lead Contact, Lawrence Miller (lwm2006@uic.edu).

Materials Availability

Plasmids generated in this study will be deposited to Addgene. Detailed information on experiments can be found in the accompanying Transparent Methods.

Data and Code Availability

This study did not generate new code. All relevant data are available from the Lead Contact upon reasonable request.

METHODS

All methods can be found in the accompanying Transparent Methods supplemental file.

SUPPLEMENTAL INFORMATION

Supplemental Information can be found online at https://doi.org/10.1016/j.isci.2020.101533.

ACKNOWLEDGMENTS

We thank Lumiphore, Inc. for providing Lumi4-Tb and TMP-Lumi4-R_9. Funding was provided by NIGMS (R01 GM081030), the UIC CCTS (NIH U54TR001354) and the UICentre for Drug Discovery (award no. 2017-03), University of Illinois at Chicago.

AUTHOR CONTRIBUTIONS

Conceptualization, L.W.M.; Methodology, T.C., H.P., and L.W.M.; Investigation, T.C. and H.P.; Resources, T.C., H.P., and A.M.; Writing – Original Draft, T.C. and L.W.M.; Writing – Review and Editing, T.C., H.P., and L.W.M.; Visualization, T.C., H.P., and L.W.M.; Supervision, Project Administration, and Funding Acquisition, L.W.M.

DECLARATION OF INTERESTS

The authors declare no competing interests.

Received: June 25, 2020
Revised: August 23, 2020
Accepted: September 2, 2020
Published: September 25, 2020

REFERENCES

Afsari, H.S., Cardoso Dos Santos, M., Lindén, S., Chen, T., Qiu, X., van Bergen en Henegouwen, P.M.P., Jennings, T.L., Susumu, K., Medintz, I.L., Hildebrandt, N., et al. (2016). Time-gated FRET nanoassemblies for rapid and sensitive intra- and extracellular fluorescence imaging. Sci. Adv. *2*, e1600265.

Allen, M.D., and Zhang, J. (2006). Subcellular dynamics of protein kinase A activity visualized by FRET-based reporters. Biochem. biophys. Res. Commun. *348*, 716–721.

Arai, R., Ueda, H., Kitayama, A., Kamiya, N., and Nagamune, T. (2001). Design of the linkers which effectively separate domains of a bifunctional fusion protein. Protein Eng. Des. Selection *14*, 529–532.

Aulsebrook, M.L., Graham, B., Grace, M.R., and Tuck, K.L. (2018). Lanthanide complexes for luminescence-based sensing of low molecular weight analytes. Coord. Chem. Rev. *375*, 191–220.

Banaszynski, L.A., Liu, C.W., and Wandless, T.J. (2005). Characterization of the FKBP.rapamycin.FRB ternary complex. J. Am. Chem. Soc. *127*, 4715–4721.

Cardoso Dos Santos, M., Colin, I., Ribeiro Dos Santos, G., Susumu, K., Demarque, M., Medintz, I.L., and Hildebrandt, N. (2020). Time-gated FRET nanoprobes for autofluorescence-free long-term in vivo imaging of developing zebrafish. Adv. Mater. 2003912.

Cho, U., Riordan, D.P., Ciepla, P., Kocherlakota, K.S., Chen, J.K., and Harbury, P.B. (2018). Ultrasensitive optical imaging with lanthanide lumiphores. Nat. Chem. Biol. *14*, 15–21.

Comps-Agrar, L., Kniazeff, J., Brock, C., Trinquet, E., and Pin, J.P. (2012). Stability of GABAB receptor oligomers revealed by dual TR-FRET and drug-induced cell surface targeting. FASEB J. *26*, 3430–3439.

Delbianco, M., Sadovnikova, V., Bourrier, E., Mathis, G., Lamarque, L., Zwier, J.M., and Parker, D. (2014). Bright, highly water-soluble triazacyclononane europium complexes to detect ligand binding with time-resolved FRET microscopy. Angew. Chem. Int. Ed. Engl. *53*, 10718–10722.

Eyckerman, S., Lemmens, I., Catteeuw, D., Verhee, A., Vandekerckhove, J., Lievens, S., and Tavernier, J. (2005). Reverse MAPPIT: screening for protein-protein interaction modifiers in mammalian cells. Nat. Methods *2*, 427–433.

Faklaris, O., Cottet, M., Falco, A., Villier, B., Laget, M., Zwier, J.M., Trinquet, E., Mouillac, B., Pin, J.-P., and Durroux, T. (2015). Multicolor time-resolved Förster resonance energy transfer microscopy reveals the impact of GPCR oligomerization on internalization processes. FASEB J. *29*, 2235–2246.

Fletcher, S., and Hamilton, A.D. (2007). Protein-protein interaction inhibitors: small molecules from screening techniques. Curr. Top. Med. Chem. *7*, 922–927.

Herce, H.D., Deng, W., Helma, J., Leonhardt, H., and Cardoso, M.C. (2013). Visualization and targeted disruption of protein interactions in living cells. Nat. Commun. *4*, 2660.

Hildebrandt, N., Wegner, K.D., and Algar, W.R. (2014). Luminescent terbium complexes: superior Förster resonance energy transfer donors for flexible and sensitive multiplexed biosensing. Coord. Chem. Rev. *273-274*, 125–138.

Iversen, P.W., Eastwood, B.J., Sittampalam, G.S., and Cox, K.L. (2006). A comparison of assay performance measures in screening assays: signal window, Z' factor, and assay variability ratio. J. Biomol. Screen. *11*, 247–252.

Komatsu, N., Aoki, K., Yamada, M., Yukinaga, H., Fujita, Y., Kamioka, Y., and Matsuda, M. (2011). Development of an optimized backbone of FRET biosensors for kinases and GTPases. Mol. Biol. Cell *22*, 4647–4656.

Korn, K., and Krausz, E. (2007). Cell-based high-content screening of small-molecule libraries. Curr. Opin. Chem. Biol. *11*, 503–510.

Lam, A.J., St-Pierre, F., Gong, Y., Marshall, J.D., Cranfill, P.J., Baird, M.A., McKeown, M.R., Wiedenmann, J., Davidson, M.W., Schnitzer, M.J., et al. (2012). Improving FRET dynamic range with bright green and red fluorescent proteins. Nat. Methods *9*, 1005–1012.

Linden, S., Singh, M.K., Wegner, K.D., Regairaz, M., Dautry, F., Treussart, F., and Hildebrandt, N. (2015). Terbium-based time-gated Forster resonance energy transfer imaging for evaluating protein-protein interactions on cell membranes. Dalton Trans. *44*, 4994–5003.

Lundholt, B.K., Heydorn, A., Bjorn, S.P., and Praestegaard, M. (2006). A simple cell-based HTS assay system to screen for inhibitors of p53-Hdm2 protein-protein interactions. Assay Drug Dev. Technol. *4*, 679–688.

Mathieu, E., Sipos, A., Demeyere, E., Phipps, D., Sakaveli, D., and Borbas, K.E. (2018). Lanthanide-based tools for the investigation of cellular environments. Chem. Commun. *54*, 10021–10035.

Michnick, S.W., Ear, P.H., Manderson, E.N., Remy, I., and Stefan, E. (2007). Universal strategies in research and drug discovery based on protein-fragment complementation assays. Nat. Rev. Drug Discov. *6*, 569–582.

Miller, L.W., Cai, Y., Sheetz, M.P., and Cornish, V.W. (2005). In vivo protein labeling with trimethoprim conjugates: a flexible chemical tag. Nat. Methods *2*, 255–257.

Mohandessi, S., Rajendran, M., Magda, D., and Miller, L.W. (2012). Cell-penetrating peptides as delivery vehicles for a protein-targeted terbium complex. Chemistry *18*, 10825–10829.

Nagai, T., Yamada, S., Tominaga, T., Ichikawa, M., and Miyawaki, A. (2004). Expanded dynamic range of fluorescent indicators for Ca(2+) by circularly permuted yellow fluorescent proteins. Proc. Natl. Acad. Sci. U S A *101*, 10554–10559.

New, E.J., Congreve, A., and Parker, D. (2010). Definition of the uptake mechanism and sub-cellular localisation profile of emissive lanthanide complexes as cellular optical probes. Chem. Sci. *1*, 111–118.

Pawson, T., and Nash, P. (2003). Assembly of cell regulatory systems through protein interaction domains. Science *300*, 445–452.

Petschnigg, J., Groisman, B., Kotlyar, M., Taipale, M., Zheng, Y., Kurat, C.F., Sayad, A., Sierra, J.R., Mattiazzi Usaj, M., Snider, J., et al. (2014). The mammalian-membrane two-hybrid assay (MaMTH) for probing membrane-protein interactions in human cells. Nat. Methods *11*, 585–592.

Pfleger, K.D., and Eidne, K.A. (2006). Illuminating insights into protein-protein interactions using bioluminescence resonance energy transfer (BRET). Nat. Methods *3*, 165–174.

Piston, D.W., and Kremers, G.J. (2007). Fluorescent protein FRET: the good, the bad and the ugly. Trends Biochem. Sci. *32*, 407–414.

Rajapakse, H.E., Gahlaut, N., Mohandessi, S., Yu, D., Turner, J.R., and Miller, L.W. (2010). Time-resolved luminescence resonance energy transfer imaging of protein-protein interactions in living cells. Proc. Natl. Acad. Sci. U S A *107*, 13582–13587.

Rajapakse, H.E., Reddy, D.R., Mohandessi, S., Butlin, N.G., and Miller, L.W. (2009). Luminescent terbium protein labels for time-resolved microscopy and screening. Angew. Chem. Int. Ed. Engl. *48*, 4990–4992.

Rajendran, M., Yapici, E., and Miller, L.W. (2014). Lanthanide-based imaging of protein-protein interactions in live cells. Inorg. Chem. *53*, 1839–1853.

Scott, D.E., Bayly, A.R., Abell, C., and Skidmore, J. (2016). Small molecules, big targets: drug discovery faces the protein-protein interaction challenge. Nat. Rev. Drug Discov. *15*, 533–550.

Selvin, P.R. (1996). Lanthanide-based resonance energy transfer. IEEE J. Sel. Top. Quant. Electron. *2*, 1077–1087.

Selvin, P.R. (2002). Principles and biophysical applications of lanthanide-based probes. Annu. Rev. Biophys. Biomol. Struct. *31*, 275–302.

Shangary, S., and Wang, S. (2009). Small-molecule inhibitors of the MDM2-p53 protein-protein interaction to reactivate p53 function: a novel approach for cancer therapy. Annu. Rev. Pharmacol. Toxicol. *49*, 223–241.

Sivaramakrishnan, S., and Spudich, J.A. (2011). Systematic control of protein interaction using a modular ER/K alpha-helix linker. Proc. Natl. Acad. Sci. U S A *108*, 20467–20472.

Song, Y., Madahar, V., and Liao, J. (2011). Development of FRET assay into quantitative and high-throughput screening technology platforms for protein-protein interactions. Ann. Biomed. Eng. *39*, 1224–1234.

Specht, E.A., Braselmann, E., and Palmer, A.E. (2017). A critical and comparative Review of fluorescent tools for live-cell imaging. Annu. Rev. Physiol. *79*, 93–117.

Stroik, D.R., Yuen, S.L., Janicek, K.A., Schaaf, T.M., Li, J., Ceholski, D.K., Hajjar, R.J., Cornea, R.L., and Thomas, D.D. (2018). Targeting protein-protein interactions for therapeutic discovery via FRET-based high-throughput screening in living cells. Sci. Rep. *8*, 12560.

Swanson, C.J., and Sivaramakrishnan, S. (2014). Harnessing the unique structural properties of isolated alpha-helices. J. Biol. Chem. *289*, 25460–25467.

Vassilev, L.T., Vu, B.T., Graves, B., Carvajal, D., Podlaski, F., Filipovic, Z., Kong, N., Kammlott, U., Lukacs, C., Klein, C., et al. (2004). In vivo activation of the p53 pathway by small-molecule antagonists of MDM2. Science *303*, 844–848.

Welch, C.M., Elliott, H., Danuser, G., and Hahn, K.M. (2011). Imaging the coordination of multiple signalling activities in living cells. Nat. Rev. Mol. Cell Biol. *12*, 749–756.

Yapici, E., Reddy, D.R., and Miller, L.W. (2012). An adaptable luminescence resonance energy transfer assay for measuring and screening protein-protein interactions and their inhibition. Chembiochem *13*, 553–558.

You, X., Nguyen, A.W., Jabaiah, A., Sheff, M.A., Thorn, K.S., and Daugherty, P.S. (2006). Intracellular protein interaction mapping with FRET hybrids. Proc. Natl. Acad. Sci. U S A *103*, 18458–18463.

Zhang, K.Y., Yu, Q., Wei, H., Liu, S., Zhao, Q., and Huang, W. (2018). Long-lived emissive probes for time-resolved photoluminescence bioimaging and biosensing. Chem. Rev. *118*, 1770–1839.

Zou, X., Rajendran, M., Magda, D., and Miller, L.W. (2015). Cytoplasmic delivery and selective, multicomponent labeling with oligoarginine-linked protein tags. Bioconjug. Chem. *26*, 460–465.

Zwier, J.M., Bazin, H., Lamarque, L., and Mathis, G. (2014). Luminescent lanthanide cryptates: from the bench to the bedside. Inorg. Chem. *53*, 1854–1866.

iScience, Volume *23*

Supplemental Information

Single-Chain Lanthanide Luminescence Biosensors for Cell-Based Imaging and Screening of Protein-Protein Interactions

Ting Chen, Ha Pham, Ali Mohamadi, and Lawrence W. Miller

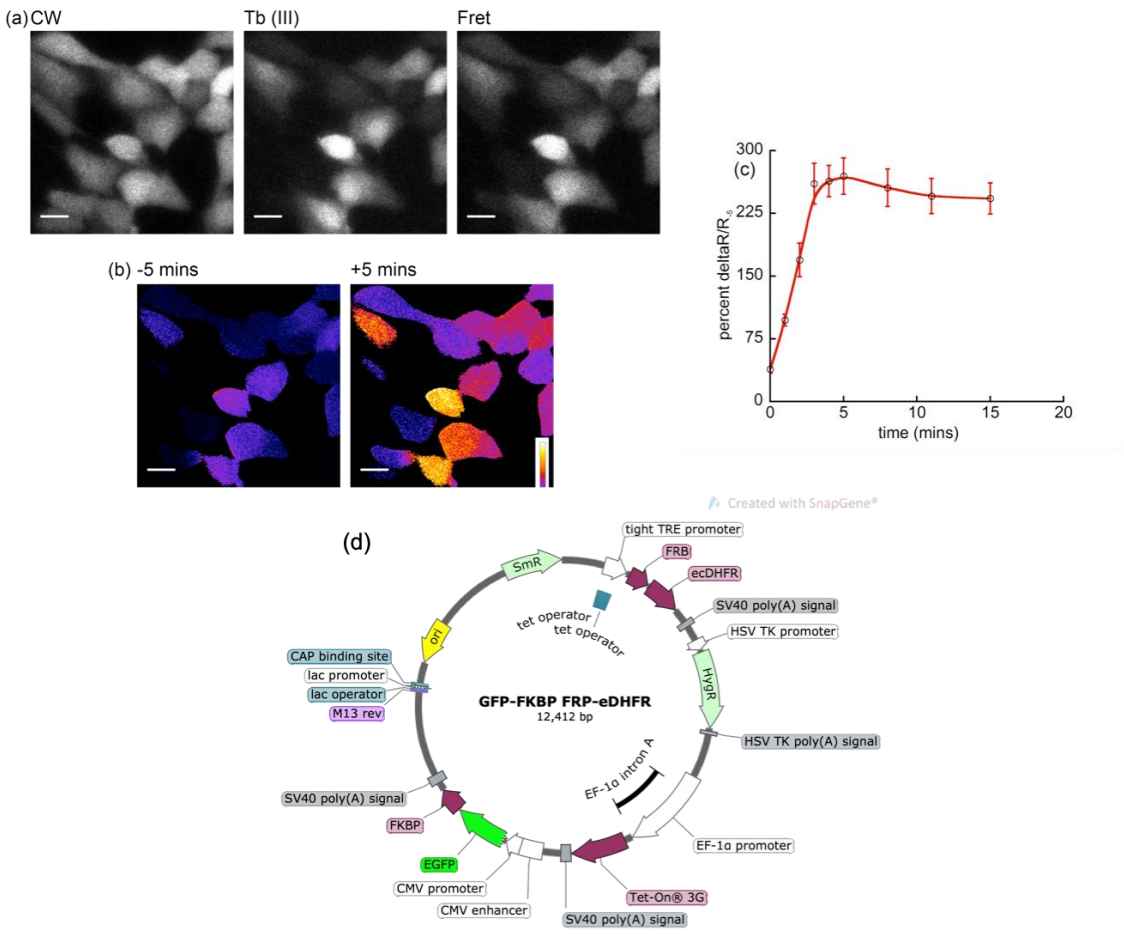

Figure S1. **Time-gated luminescence microscopy of a dual-chain, FKBP12/FRB LRET biosensor.** ***Related to Figure 3.*** (a) Representative images of NIH3T3 fibroblasts cells stably expressing pPBH-TRE$_{tight}$-FRB-eDHFR/CMV-EGFP-FKBP12. Micrographs: CW, steady-state fluorescence (λ_{ex}, 480 nm; λ_{em}, 535 nm); Tb(III), time-gated Tb(III) luminescence (λ_{ex}, 365 nm; λ_{em}, 620 nm/20; gate delay 10 μs); LRET, time-gated Tb(III)-to-GFP sensitized emission (λ_{ex}, 365 nm; λ_{em}, 520/20 nm, gate delay 10 μs). Scale bar, 20 μm. (b) Ratio images (LRET/GFP) before (left) and after (right) addition of rapamycin. (c) Percent increase of LRET/GFP at different time points after adding rapamycin ($\Delta R/R_{-5}$). Values given are averaged from 11 cells. Error bars, SEM. (d) Schematic of a dual-promoter PiggyBac plasmid vector encoding the fusion protein EGFP- FKBP12 under control of a CMV promoter for constitutive expression and FRB-eDHFR under control of a pTREtight promoter for doxycycline-induced expression.

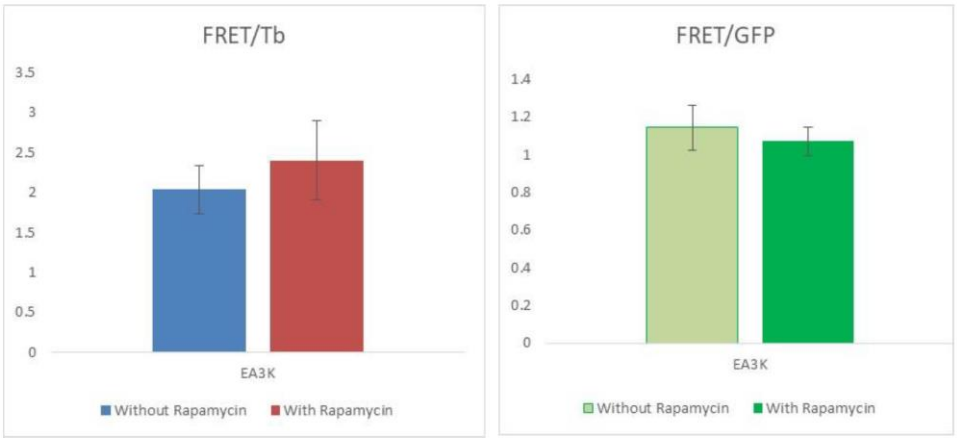

Figure S2 No significant FRET changes observed in cells expressing an FKBP/FRB sensor that incorporates a EAAAK repeat linker. *Related to Figure 3.* NIH 3T3 fibroblasts stably expressing pPBH-TRE$_{tight}$-FRB-eDHFR-(EAAAK)$_{20nm}$-EGFP-FKBP12 were incubated in medium containing TMP-Lumi4-R$_9$ (12 µM) for 15 min at 37 °C, washed 1X with PBS, reimmersed in imaging medium with or without rapamycin (1 µM), incubated for 15 min at 37 °C and imaged using TGL microscopy. Images were acquired of steady-state fluorescence (λ_{ex}, 480/20 nm; λ_{em}, 535/30 nm), time-gated Tb(III) luminescence (λ_{ex}, 365 nm; λ_{em}, 620 nm/20; gate delay 10 µs) and time-gated Tb(III)-to-GFP sensitized emission (λ_{ex}, 365 nm; λ_{em}, 520/20 nm, gate delay 10 µs). Mean gray values were measured in corresponding regions of interest (ROI) of multiple cells (n = ≥13 cells for each condition) in each channel, and ratios (FRET/GFP, FRET/Tb) were recorded for each ROI. Graphs represent mean ratio values. Error bars, SEM. The experiment was repeated twice more on different days, and results were similar (no significant FRET changes observed).

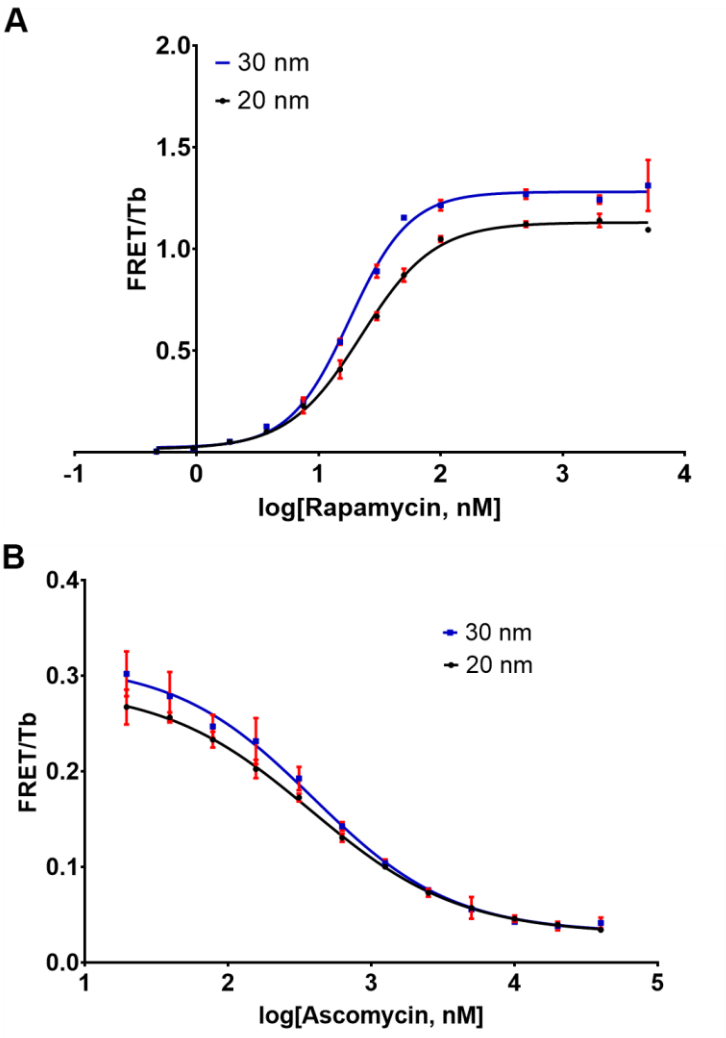

Figure S3. **Rapamycin and ascomycin titration assay**. ***Related to Figure 4.*** NIH 3T3 cells expressing FKBP/FRB biosensors (containing 20 nm or 30 nm ER/K linkers) were seeded into 96-well plates. Following overnight incubation, cells were treated with lysis buffer containing TMP-Lumi4-Tb (50 nM) and (A) serial dilutions of rapamycin (final conc., 5 μM to 0.5 nM) or (B) 0.333 μM rapamycin and a serial dilutions of ascomycin (final conc., 40 μM to 0.02 μM). Values represent mean, background-corrected FRET/Tb ratios from 8 or more wells for each condition, error bars, SD. See Methods for further details.

TRANSPARENT METHODS

Materials. Dulbecco's modified eagle medium with 1g/L glucose (DMEM, 10-014CV), Dulbecco's modified eagle medium with 4.5g/L glucose (DMEM, 10-013CV), Dulbecco's phosphate buffer saline (DPBS, 21-030 and 21-031), 0.25% trypsin/2.21 mM EDTA and 0.05% trypsin/2.21 mM EDTA (25-053-CI) were purchased from Corning cellgro®. MEM non-essential amino acid (11140), DMEM (without phenol red, 21063), HEPES (15630-080) and Lipofectamine 2000 (11668-027) were purchased from Invitrogen™. FBS (S11150) was purchased from Atlanta Biologicals. Hygromycin (sc-29067) and Nutlin-3 (sc45061) were purchased from Santa Cruz Biotechnology. BSA (700-107P) was purchase from Gemini Bio-products. Rapamycin (553211-500UG) was purchased from Millipore. Ascomycin (11309) was purchase from Cayman Chemical. NADPH (N0411) and doxycycline (D9891) were purchased from Sigma. DMSO (D128-500) was purchased from Fisher Chemical. Patent V blue sodium salt (21605) was purchased from Fluka. Clonetech In-fusion cloning kit (638909) was purchased from Takara. All enzymes and buffers used in cloning were purchased from New England Biolabs.

Luminescent Tb(III) complexes. Heterodimers of trimethoprim linked to luminescent Tb(III) complexes (TMP-cs124-TTHA,(Rajapakse, et al., 2009; Reddy, et al., 2011) and TMP-Lumi4,(Rajapakse, et al., 2009)) and a cell permeable variant conjugated to oligoarginine, TMP-Lumi4-R_9 (Mohandessi, et al., 2012), were prepared as previously reported.

Plasmids. All DNA constructs were sequenced by the UIC Research Resources Center (RRC).

pPBH-TRE_{tight}-FRB-eDHFR/CMV-EGFP-FKBP12, encoding the doxycycline-inducible expression of FRB-eDHFR and constitutive expression of EGFP-FKBP12 was described in Yapici.(Yapici, 2017) The gene encoding FKBP12 was subcloned from plasmid pRSETb-GFP-FKBP(Yapici, et al., 2012) to pEGFP-Claudin(Rajapakse, et al., 2010) to generate pEGFP-FKBP. A 321 bp fragment encoding FKBP12 was amplified by PCR from pRSETb-GFP-FKBP using the primers 5' – CT GGA AGT GCT GCT CGA GGA GTG CAG GTG G – 3' (XhoI, coding strand) and 5' – GCA GCC GGA TCA AGC TCT AGA TTA TTC CAG TTT TAG AAG CTCC – 3' (XbaI, non-coding strand). This fragment was inserted between the XhoI site and the XbaI site in pEGFP-Claudin with In-Fusion® Cloning Kit to give to pEGFP-FKBP.

The gene encoding FRB-eDHFR was subcloned from plasmid pRSETb-FRB-eDHFR(Yapici, et al., 2012) to pPBH-TRE_{tight} to generate pPBH-TRE_{tight}-FRB-eDHFR. A 783 bp fragment encoding FRB-eDHFR was amplified by PCR from pRSETb-FRB-eDHFR using the primers 5' – AC TCT GCA GTC GAC GGT ACC ATG ATC CTC TGG CAT GAG ATG TGG C – 3' (KpnI, coding strand) and 5' – GA TCC CGG GCC CGC GGT ACC TCA CTA TTA CCG CCG CTC CAG AAT CTC AAA G – 3' (KpnI, non-coding strand). This fragment was inserted at the KpnI site in pPBH-TRE_{tight} with In-Fusion® Cloning Kit to give to pPBH-TRE_{tight}-FRB-eDHFR.

The gene encoding (CMV Promoter)-EGFP-FKBP-(bGH Poly(A) Signal Sequence) was subcloned from plasmid pEGFP-FKBP to pPBH-TRE_{tight}-FRB-eDHFR to generate pPBH-TRE_{tight}-FRB-eDHFR/CMV-EGFP-FKBP. A 1850 bp fragment encoding (CMV Promoter)-EGFP-FKBP-(bGH Poly(A) Signal Sequence) was amplified by PCR from pEGFP-FKBP using the primers 5' – GCCCGTCCCACCAGGTGAGTTCCGCGTTACATAACTTACG – 3' (SexAI, coding strand) and 5' – CGCCTGTTGACCTGGTCGCGTTAAGATACATTGATGAG – 3' (SexAI, non-coding strand). This fragment was inserted at the SexAI site in pPBH-TRE_{tight}-FRB-

eDHFR with In-Fusion® Cloning Kit to give to pPBH-TRE$_{tight}$-FRB-eDHFR/CMV-EGFP-FKBP.

pPBH-TRE$_{tight}$-FRB-eDHFR-(ER/K)$_{10nm}$-EGFP-FKBP12 was prepared via subcloning from a pUC67 plasmid that contained the ORF, FRB-eDHFR-(ER/K)$_{10nm}$-EGFP-FKBP12. GenScript, Inc. prepared the source vector using plasmid DNA that contained the fragments EGFP-FKBP12 and FRB-eDHFR (pPBH-TRE$_{tight}$-FRB-eDHFR/CMV-EGFP-FKBP(Yapici, 2017)) and synthesized DNA encoding an ER/K linker of length 10 nm with the sequence of 5' – GAA GAG GAA GAG AAA AAA AAA CAG CAG GAA GAG GAA GCA GAA AGG CTG AGG CGT ATT CAA GAA GAA ATG GAA AAG GAA AGA AAA AGA CGT GAA GAA GAC GAA AAA CGT CGA AGA AAG GAA GAG GAG GAA AGG CGG ATG AAA CTT GAG ATG GAA GCA AAG AGA AAA CAA GAA GAA GAA GAG AGA AAG AAA AGG GAA GAT GAT GAA AAA CGC AAG AAG AAG. The ORF was inserted into the pPBH-TRE$_{tight}$ vector between KpnI site and NheI site to give pPBH-TRE$_{tight}$-FRB-eDHFR-(ER/K)$_{10nm}$ -EGFP-FKBP12.

pPBH-TRE$_{tight}$-FRB-eDHFR-(ER/K)$_{30nm}$-EGFP-FKBP12. A 630 bp (ER/K)$_{30nm}$ linker fragment (sequence reported in Sivaramakdrishnan and Spudich(Sivaramakrishnan and Spudich, 2011)) was synthesized and cloned into pUC57 vector by GenScript, Inc. The genes encoding FRB-eDHFR, (ER/K)$_{30nm}$, EGFP-FKBP12 were subcloned from plasmids pPBH-TREtight-FRB-eDHFR-(ER/K)$_{10nm}$-EGFP-FKBP12 and (ER/K)$_{30nm}$ in pUC57 to pPBH-TREtight to generate pPBH-TREtight-FRB-eDHFR-(ER/K)$_{30nm}$-EGFP-FKBP12. A 753 bp fragment encoding FRB-eDHFR was prepared by PCR from pPBH-TREtight-FRB-eDHFR-(ER/K)$_{10nm}$-EGFP-FKBP12 using the primers 5'-ACT CTG CAG TCG ACG GTA CCA TGA TCC TCT GGC ATG AGA TGT GGC -3' (coding strand) and 5'-TCG GAT CCT CCG CTT CCC CGC CG -3' (non-coding strand). A 630 bp fragment encoding (ER/K)$_{30nm}$ was prepared by PCR from (ER/K)$_{30nm}$ in pUC57 using the primers 5'-AAG CGG AGG ATC CGA AGA GGA GGA GAA AAA GAA GGA -3' (coding strand) and 5'-CCA GAG CCA CCG GTT CTC TGT TTT CGC TCT GC -3' (non-coding strand). A 1041 bp fragment encoding EGFP-FKBP12 was prepared by PCR from pPBH-TREtight-FRB-eDHFR-(ER/K)$_{10nm}$-EGFP-FKBP12 using the primers 5'-AAC CGG TGG CTC TGG CAT GGT GAG CA -3' (coding strand) and 5'-ATG CGG CCG CGC TAG-3' (non-coding strand). These 3 fragments were inserted between the KpnI site and the NheI site in pPBH-TREtight by Clontech In-Fusion® Cloning Kit to get pPBH-TREtight-FRB-eDHFR-(ER/K)$_{30nm}$-EGFP-FKBP12.

pPBH-TRE$_{tight}$-FRB-eDHFR-(ER/K)$_{20nm}$-EGFP-FKBP12. The (ER/K)$_{20nm}$ linker is comprised of the first 396 bp of the (ER/K)$_{30nm}$ linker. The genes encoding FRB-eDHFR, (ER/K)$_{20nm}$, EGFP-FKBP12 were subcloned from plasmids pPBH-TREtight-FRB-eDHFR-(ER/K)$_{10nm}$-EGFP-FKBP12 and (ER/K)$_{30nm}$ in pUC57 to pPBH-TREtight to generate pPBH-TREtight-FRB-eDHFR-(ER/K)$_{20nm}$-EGFP-FKBP12. A 753 bp fragment encoding FRB-eDHFR was prepared by PCR from pPBH-TREtight-FRB-eDHFR-(ER/K)$_{10nm}$-EGFP-FKBP12 using the primers 5'-ACT CTG CAG TCG ACG GTA CCA TGA TCC TCT GGC ATG AGA TGT GGC -3' (coding strand) and 5'-TCG GAT CCT CCG CTT CCC CGC CG -3' (non-coding strand). A 396 bp fragment encoding (ER/K)$_{20nm}$ was prepared by PCR from (ER/K)$_{30nm}$ in pUC57 using the primers 5'-AAG CGG AGG ATC CGA AGA GGA GGA GAA AAA GAA GGA -3' (coding strand) and 5'-CCA GAG CCA CCG GTC TCT TCC TTG GCC TTT TTC TCC TGC -3' (non-coding strand). A 1041 bp fragment encoding EGFP-FKBP12 was prepared by PCR from pPBH-TREtight-FRB-eDHFR-(ER/K)$_{10nm}$ -EGFP-FKBP12 using the primers 5'-GAA GAG ACC GGT GGC TCT GGC ATG GTG AGC A -3' (coding strand) and 5'-ATG CGG CCG CGC TAG-3' (non-coding strand). These 3 fragments were inserted between the KpnI site and the NheI site in

pPBH-TRE_{tight} by Clontech In-Fusion® Cloning Kit to get pPBH-TRE_{tight}-FRB-eDHFR-$(ER/K)_{20nm}$ -EGFP-FKBP12.

pPBH-TRE_{tight}-p53(1-92)-eDHFR-$(ER/K)_n$-EGFP-HDM2(1-128). The genes encoding p53(1-92), FRB-eDHFR-$(ER/K)_n$-EGFP (n=10 nm, 20nm or 30 nm), and HDM2 (1-128) were subcloned from plasmids p53-GFP, pPBH-TRE_{tight}-FRB-eDHFR-$(ER/K)_n$-EGFP-FKBP12 (n = 10 nm, 20nm or 30 nm) and pCMV-HDM2(C464A) to pPBH-TRE_{tight} to generate pPBH-TRE_{tight}-p53(1-92)-eDHFR-$(ER/K)_n$-EGFP-HDM2(1-128). A 276 bp fragment encoding p53 (residues 1-92) was prepared by PCR from p53-GFP using the primers 5'-ACT CTG CAG TCG ACG GTA CCA TGG AGG AGC CGC AGT CA -3' (coding strand) and 5'-CCA GAT CCG GGC CAG GAG GGG G -3' (non-coding strand). Fragments of length 1446 bp, 1620 bp, or 1845 bp that encoded eDHFR-$(ER/K)_n$-EGFP where n equaled 10 nm, 20nm or 30 nm, respectively, were prepared by PCR from pPBH-TREtight-FRB-eDHFR-(ER/K)n-EGFP-FKBP12 (n=10 nm, 20nm or 30 nm) using the primers 5'-CTG GCC CGG ATC TGG AGG ATC TGG AAT CAG TC -3' (coding strand) and 5'-TTG CAC ATT CGA GAT CTG AGT CCG GAC TTG TA -3' (non-coding strand). A 384 bp fragment encoding HDM2 (residues 1-128) was prepared by PCR from pCMV-HDM2(C464A) using the primers 5'-ATC TCG AAT GTG CAA TAC CAA CAT GTC TGT ACC -3' (coding strand) and 5'-ATG CGG CCG CGC TAG CCT ATT CAA GGT GAC ACC TGT TCT CAC TC -3' (non-coding strand). These 3 fragments were inserted between the KpnI site and the NheI site in pPBH-TRE_{tight} using Clontech In-Fusion® Cloning Kit to obtain pPBH-TRE_{tight}-p53(1-92)-eDHFR-$(ER/K)_n$-EGFP-HDM2(1-128) (n=10 nm, 20nm or 30 nm).

pPBH-TRE_{tight}-FRB-eDHFR-$(EAAAK)_{20nm}$-EGFP-FKBP12 was prepared via subcloning from a pUC67 plasmid that contained the ORF, FRB-eDHFR-$(EAAAK)_{20nm}$-EGFP-FKBP12. GenScript, Inc. prepared the source vector using the plasmid, pUC67-FRB-eDHFR-$(ER/K)_{10nm}$ -EGFP-FKBP12 and synthesized DNA encoding an EAAAK linker of length ~20 nm with the sequence of 5' – $(EAAAK)_{27}$. The ORF was inserted into the pPBH-TRE_{tight} vector between KpnI site and NheI site to give pPBH-TRE_{tight}-FRB-eDHFR-$(ER/K)_{10nm}$ -EGFP-FKBP12.

Stable expression of biosensor plasmids.

All FRB/FKBP12 biosensor plasmids were transfected to NIH 3T3 cells, while all p53/HDM2 biosensors were transfected to Hela cells. Cells were grown to 70-80% confluency in a sterile 10 cm dish. The cells were transfected with 12 µg of biosensor plasmid DNA and the recombination helper plasmid pSPB-Transposase with a Lipofectamine:plasmid ratio of 2.5µL:1µg per plasmid. Plasmid and Lipofectamine solutions were first prepared in separate microcentrifuge tubes in OptiMEM I with a total volume of 1.5 mL. After 5 minutes of incubation at room temperature, the solutions were mixed and kept at room temperature for an additional 20 minutes. The media in 10 cm dish was aspirated and the Lipofectamine and plasmids solution was added into it. The cells were incubated with the solution for 4 hours at 37 °C with 5% CO_2, and then the solution was replaced with 10 mL of fresh DMEM(+) (DMEM supplied with 15 mM HEPES, 10% FBS and 100 mg/mL Hygromycin). The transfections were confirmed with microscopy and/or flow cytometry by using the GFP emissions.

Probe delivery for time-gated luminescence microscopy.

Cells were trypsinized and seeded at 20,000 cells/well in an 8-well chambered coverglass (Nunc™, 12-565-470) with fresh DMEM (+) containing 100 ng/mL

doxycycline to induce the expression of proteins and incubated at 37 °C and 5% CO_2 overnight. For FRB/FKBP12 stable transfected cell lines, on the following day the cells were washed twice with DPBS (+Ca/+Mg), 100 µL of TMP-Lumi4-R9 (12 µM in DMEM without phenol red) was added, and the cells were incubated for 15 min at room temperature. Cells were washed again with DPBS (+Ca/+Mg) and 150 µL of DMEM without phenol with Rapamycin (1 µM, 1% DMSO) was added. Control wells received DMEM without phenol red with DMSO (1%) but without rapamycin. The cells were incubated for 15 min at 37 °C and 5% CO_2. Immediately prior to microscope imaging, 20µL of 10 mM patent blue V solution (final concentration: 1 mM) was added to quench extracellular luminescence from non-specifically adsorbed probe. To obtain the time-lapse images of FRB/FKBP12 interaction, cells were first loaded with TMP-Lumi4-R_9, washed, immersed in DMEM (without phenol red) with patent blue (1 mM) and then rapamycin was added (final concentration: 2 µM).

HeLa cells stably expressing the p53/HDM2 biosensor were seeded into chambered coverglass (20,000 cells/well) and incubated overnight in DMEM with 100 ng/mL to induce protein expression. On the day after seeding, the cells were incubated with DMEM without FBS containing Nutlin-3 (final conc. 10 µM) or vehicle (DMSO). for 90 min at 37 °C and 5% CO_2. The cells were washed twice with DPBS (+Ca/+Mg), 100 µL of TMP-Lumi4-R9 (12 µM in DMEM without phenol red) was added, and the cells were incubated for 20 min at room temperature. Cells were washed again with DPBS (+Ca/+Mg) and 150 µL of patent blue V solution (1 mM in DMEM without phenol red, containing 10 µM Nutlin-3) was added to the sample well for microscope imaging.

Time-gated Luminescence Microscopy and image processing.

Time-gated luminescence images were acquired using a previously described epi-fluorescence microscope (Axiovert 200, Carl Zeiss, Inc.).(Gahlaut and Miller, 2010; Rajendran and Miller, 2015) For each time-gated image acquisition, the signal from multiple excitation/emission events was accumulated on the ICCD sensor and read out at the end of the camera frame. The UV LED pulse width and pulse period, the intensifier delay time and on-time, the camera frame length (66.67 ms – 2 s) and the intensifier gain voltage could be varied independently. The source/camera timing parameters were the same for all of the time-resolved images and data presented here: excitation pulse width, 1500 µs, pulse period, 3000 µs, delay time, 10 µs, intensifier on-time, 1480 µs. All data reported here was acquired at an intensifier gain of 833 V. The camera control software enabled summation of multiple frames to yield a single composite .TIFF image with a bit depth equal to 1024 multiplied by the number of frames. All images reported here were summations of four frames (bit depth, 4096), and a feature of the camera control software was enabled that removes large variations in signal resulting from ion-feedback noise of the intensifier.

Raw, 12-bit images were imported into NIH ImageJ (v1.42q) for all processing operations including cropping, contrast adjustment, and quantitative analysis.(Schneider, et al., 2012) For each channel, 20 dark frames and 20 bright field images were stacked, converted to 32 bits, and median-filtered (radius 1), and each stack was averaged. The flat-field average was divided by the mean intensity of its central nine pixels to generate a normalized flat-field image. For each sample image, a median filter (radius 1) was applied and the master dark frame was subtracted. The resulting image was then divided by the normalized, master flat-field image, and the mean value of the detector offset was added back to the image. For ratiometric images and measurements, a binary mask was created by first averaging a series of GFP images and then applying a threshold to highlight only regions exhibiting signal. The mask was applied to

background-subtracted time-gated LRET images, and the LRET images were then divided by the GFP or Tb image. Intensity-modulated ratiometric displays were generated using the Fire lookup table in ImageJ.

Multi-well plate assays.

Time-gated luminescence measurements using multiwell plates were carried out on a PerkinElmer Victor 3V multilabel counter with the settings of delay time, 0.2 ms; window time (counting time), 0.7 ms; cycling time, 1.2 ms; excitation wavelength, 340 nm (60 nm bandpass); and emission wavelengths, 520 nm (20 nm bandpass, Tb(III)-to-GFP LRET) and 615 nm (17 nm bandpass, Tb(III) luminescence). For each experiment, a given plate was prepared with a set of blank wells (96-well plates, n = 8 or 16; 384-well plates, n = 16 or 32) that contained buffer, Tb(III) reagent and, in some cases, non-expressing cells. The signal from blank wells was used for background subtraction (see Data Analysis, below). For a given sensor-expressing cell line, each plate contained positive and negative control wells (96-well plates, n = 8 or 16; 384-well plates, n = 16 or 32) that contained cells and reagents, and either included stimulant or inhibitor (positive controls or did not (negative controls). Usually, multiple sensors were analyzed together in a single plate (e.g., FKBP/FRB sensors with 10, 20 or 30 nm ER/K linkers).

Rapamycin stimulation assay with permeabilized mammalian cells. NIH3T3 fibroblasts stably expressing pPBH-TRE_{tight}-FRB-eDHFR-$(ER/K)_n$-EGFP-FKBP12 (n = 10 nm, 20 nm or 30 nm) were seeded into multiwell plates at a density of 1.6×10^5 cells/mL (250 µL for 96-well plate, 50 µL for 384-well plate) and incubated (37 ^oC, 5% CO_2) for 24 h in culture medium containing 100 ng/mL doxycycline. For the titration assay, growth media was removed carefully with a hand pipette, and 50 µL lysis buffer (5 µM NADPH, 0.1% BSA, 0.1% Triton X-100 in DPBS) containing TMP-Lumi4 (50 nM) and rapamycin (0.47 – 5 µM) was added into the wells. For single-point assays, growth media in the wells were discarded carefully and lysis buffer with TMP-cs124-TTHA (25 nM) and either vehicle (0.25% DMSO) or rapamycin (1 µM, 0.25% DMSO) was added into the wells (50 µL for 96-well plates, 30 µL for 384-well plates). The plates were kept at room temperature in dark for 15 min prior to the first measurement. Blank wells contained lysis buffer with Tb(III) complex but no cells.

Ascomycin inhibition assay with permeabilized mammalian cells. NIH 3T3 fibroblasts stably expressing pPBH-TRE_{tight}-FRB-eDHFR-$(ER/K)_n$-EGFP-FKBP12 (n = 10 nm, 20 nm or 30 nm) were prepared as above. Lysis buffer containing TMP-cs124-TTHA (50 nM), rapamycin (333 nM) and ascomycin (final conc. 0.02 µM – 40 µM for titration assay; 20 µM for single point inhibition assay) was added into wells (50 µL for 96-well plate, 30 µL for 384-well plate). The plate was kept at room temperature in dark for 20 minutes prior to the first measurement. Blank wells contained cells without protein expression, but the same lysis buffer as sample wells.

Nutlin-3 inhibition assay with permeabilized mammalian cells. pPBH-TRE_{tight}-p53(1-92a.a.)-eDHFR-$(ER/K)_n$-EGFP-HDM2(1-128a.a.) (n = 10 nm, 20 nm or 30 nm) stably transfected HeLa cells were seeded at a density of 1.6×10^5 cells/well in a multi-well plate and incubated (37 ^oC, 5% CO_2) for 24 h in culture medium (250 µL for 96-well plate, 50 µL for 384-well plate) containing 100 ng/mL doxycycline. The following day, for the titration assay, growth media in the wells were discarded carefully and lysis buffer (50 nM TMP-cs124-TTHA-Tb^{3+}, 5 µM NADPH, 0.1% BSA, 0.1% Triton X-100, and Nutlin-3 with 2-fold serial dilution in the range of 200 µM – 0.098 µM in DPBS solution) was added into the wells. For the inhibition assay, growth media in the wells were discarded carefully and lysis buffer (50 µL for 96-well plate, 30 µL for 384-well plate; 5

μM NADPH, 0.1% BSA, 0.1% Triton X-100 in DPBS) containing 50 nM TMP-cs124-TTHA-Tb^{3+} and either vehicle (0.25% DMSO) or Nutlin-3 (10 μM, 0.25% DMSO) was added into the wells. Then the plate was kept at room temperature in dark for 20 minutes and the first measurement was taken afterwards. Blank wells contained cells without protein expression, but the same lysis buffer as sample wells.

Nutlin-3 inhibition assay with live mammalian cells. HeLa cells stably expressing pPBH-TRE_{tight}-p53(1-92)-eDHFR-$(ER/K)_n$-EGFP-HDM2(1-128) (n=20 nm or 30 nm) were grown in 96-well plates, and protein expression was induced in the same manner described above for NIH 3T3 cells. The cells were incubated at room temperature for 30 min in DMEM without phenol red containing TMP-Lumi4-R_9 (10 μM). The medium was removed, cells were washed 2X with DPBS, and DMEM (without phenol red) containing Nutlin-3 (10 μM, 0.25% DMSO) or vehicle (0.25% DMSO) was added into the wells. The plate was kept at room temperature in dark for 40 minutes prior to the first measurement. Blank wells contained cells without protein expression, but the same solutions as sample wells.

Quantification and Statistical Analysis.

Microscope data. Quantitative evaluation of LRET signal changes was performed using flat-field- and bias-corrected images of each channel: steady-state fluorescence; time-gated Tb(III) luminescence; and time-gated Tb(III)-to-GFP luminescence (LRET; see Methods section describing image processing, above). Equivalent regions of interest (ROIs) were drawn within the cytoplasm of corresponding cells in each channel image, and the mean, pixel-wise intensity within each ROI was recorded using ImageJ. A mean background value measured in ROIs outside cells was subtracted from the mean value of each cellular ROI. In all cases, ROIs from at least 10 cells were measured (specific numbers indicated in main text). The mean intensities from each set of background-subtracted ROIs were averaged for each channel, and the average values were divided to obtain LRET ratios (i.e., LRET/Tb, LRET/GFP). Standard error of the mean was calculated with error propagation. Each experimental condition was tested on at least three different days, and the data presented represents the maximum values recorded on a given day. I.e., data from different days was not combined.

Multiwell plate data analysis. The Tb(III) emission (615 nm) and Tb(III)-to-GFP sensitized emission (LRET, 520 nm) signals were measured for each plate. The LRET signal for blank cells that contained buffers, Tb(III) reagents and sometimes non-expressing cells (but never sensor-expressing cells) was averaged. The mean LRET background was subtracted from the measured LRET value of each individual sample well to obtain background-corrected LRET signals. The background-corrected LRET signals were divided by the corresponding Tb(III) signals to obtain LRET/Tb ratios. Means and standard deviations were calculated from the sets of calculated ratios for a given plate. Each experimental condition was tested on at least three different days. The results from plates with the highest quality data and estimated *Z'* values were presented in the figures and main text of the paper (i.e., data from different plates/days was not combined).

Estimation of LRET R_0 values for EGFP and TMP-Tb(III) complexes. The overlap integral J was calculated according to Eqn. 1,

$$J = \frac{\sum_i F_D(\lambda_i) \cdot \varepsilon_A(\lambda_i) \cdot \lambda_i^4}{\sum_i F_D(\lambda_I)} \qquad \text{Eqn. (1)}$$

where $F_D(\lambda)$ is the fluorescence spectrum of Tb(III), $\epsilon_A(\lambda)$ the absorption spectrum of EGFP, and λ is the wavelength. The calculations were performed using a spreadsheet (Microsoft Excel),(Visser, et al., 2011) and the value of *J* was determined to be 8.00e14 $M^{-1}cm^{-1}nm^4$ for cs124-TTHA-Tb and 9.28e14 $M^{-1}cm^{-1}nm^4$ for Lumi4-Tb. Using this value for *J,* R_0 was then calculated according to

$$R_0^6 = \frac{8.785 \cdot 10^{-5} \cdot \kappa^2 \cdot \phi_D \cdot J}{n^4} \qquad \text{Eqn.(2)}$$

where κ is the orientation factor (2/3),(Haas, et al., 1978) ϕ is the quantum yield of terbium (0.6 for cs124-TTHA-Tb(Xiao and Selvin, 2001) and 0.7 for Lumi4-Tb,(Xu, et al., 2011) and *n* is the refractive index (1.33). R_0 was determined to be 0.46 nm for cs124-TTHA-TMP and 0.48 for Lumi4-Tb.

SUPPLEMENTAL REFERENCES

Gahlaut, N., and Miller, L.W. (2010). Time-resolved microscopy for imaging lanthanide luminescence in living cells. Cytometry A 77, 1113-1125.

Haas, E., Katchalski-Katzir, E., and Steinberg, I.Z. (1978). Effect of the orientation of donor and acceptor on the probability of energy transfer involving electronic transitions of mixed polarization. Biochemistry 17, 5064-5070.

Mohandessi, S., Rajendran, M., Magda, D., and Miller, L.W. (2012). Cell-penetrating peptides as delivery vehicles for a protein-targeted terbium complex. Chemistry 18, 10825-10829.

Rajapakse, H.E., Gahlaut, N., Mohandessi, S., Yu, D., Turner, J.R., and Miller, L.W. (2010). Time-resolved luminescence resonance energy transfer imaging of protein-protein interactions in living cells. Proc Natl Acad Sci U S A 107, 13582-13587.

Rajapakse, H.E., Reddy, D.R., Mohandessi, S., Butlin, N.G., and Miller, L.W. (2009). Luminescent terbium protein labels for time-resolved microscopy and screening. Angew Chem Int Ed Engl 48, 4990-4992.

Rajendran, M., and Miller, L.W. (2015). Evaluating the performance of time-gated live-cell microscopy with lanthanide probes. Biophys J 109, 240-248.

Reddy, D.R., Pedro Rosa, L.E., and Miller, L.W. (2011). Luminescent trimethoprim-polyaminocarboxylate lanthanide complex conjugates for selective protein labeling and time-resolved bioassays. Bioconjug Chem 22, 1402-1409.

Schneider, C.A., Rasband, W.S., and Eliceiri, K.W. (2012). NIH Image to ImageJ: 25 years of image analysis. Nature Methods 9, 671-675.

Sivaramakrishnan, S., and Spudich, J.A. (2011). Systematic control of protein interaction using a modular ER/K alpha-helix linker. Proc Natl Acad Sci U S A 108, 20467-20472.

Visser, A.J., Vysotski, E.S., and Lee, J. (2011). Critical Transfer Distance Determination Between FRET Pairs. In *Photbiological Sciences Online*. (

Xiao, M., and Selvin, P.R. (2001). Quantum Yields of Luminescent Lanthanide Chelates and Far-Red Dyes Measured by Resonance Energy Transfer. Journal of the American Chemical Society 123, 7067-7073.

Xu, J., Corneillie, T.M., Moore, E.G., Law, G.L., Butlin, N.G., and Raymond, K.N. (2011). Octadentate cages of Tb(III) 2-hydroxyisophthalamides: a new standard for luminescent lanthanide labels. J Am Chem Soc 133, 19900-19910.

Yapici, E. (2017). Time-Gated Luminescence Detection for High-Throughput Screening of Protein Interaction and Inhibitions, University of Illinois at Chicago.

Yapici, E., Reddy, D.R., and Miller, L.W. (2012). An adaptable luminescence resonance energy transfer assay for measuring and screening protein-protein interactions and their inhibition. Chembiochem 13, 553-558, 489.